ANNUAL REVIEWS

Exchange of Plankton, Pollutants, and Particles Across the Nearshore Region

Melissa Moulton,[1,2] Sutara H. Suanda,[3]
Jessica C. Garwood,[4] Nirnimesh Kumar,[5,*]
Melanie R. Fewings,[4] and James M. Pringle[6]

[1]Climate and Global Dynamics Laboratory, National Center for Atmospheric Research, Boulder, Colorado, USA; email: mmoulton@ucar.edu

[2]Applied Physics Laboratory, University of Washington, Seattle, Washington, USA

[3]Department of Physics and Physical Oceanography, University of North Carolina Wilmington, Wilmington, North Carolina, USA; email: suandas@uncw.edu

[4]College of Earth, Ocean, and Atmospheric Sciences, Oregon State University, Corvallis, Oregon, USA; email: jessica.garwood@oregonstate.edu, melanie.fewings@oregonstate.edu

[5]Department of Civil and Environmental Engineering, University of Washington, Seattle, Washington, USA

[6]Department of Earth Sciences and Institute for the Study of Earth, Oceans, and Space, University of New Hampshire, Durham, New Hampshire, USA; email: jpringle@unh.edu

ANNUAL REVIEWS CONNECT

www.annualreviews.org

- Download figures
- Navigate cited references
- Keyword search
- Explore related articles
- Share via email or social media

*1984–2020

OPEN ACCESS

Keywords

nearshore, cross-shore exchange, particle behavior, turbulence, wind, surface waves, internal waves

Abstract

Exchange of material across the nearshore region, extending from the shoreline to a few kilometers offshore, determines the concentrations of pathogens and nutrients near the coast and the transport of larvae, whose cross-shore positions influence dispersal and recruitment. Here, we describe a framework for estimating the relative importance of cross-shore exchange mechanisms, including winds, Stokes drift, rip currents, internal waves, and diurnal heating and cooling. For each mechanism, we define an exchange velocity as a function of environmental conditions. The exchange velocity applies for organisms that keep a particular depth due to swimming or buoyancy. A related exchange diffusivity quantifies horizontal spreading of particles without enough vertical swimming speed or buoyancy to counteract turbulent velocities. This framework provides a way to determine

which processes are important for cross-shore exchange for a particular study site, time period, and particle behavior.

1. OVERVIEW AND MOTIVATION

Plankton: drifting organisms that may swim weakly vertically, such as algae, copepods, and many larvae

Pollutants: pathogens (including bacteria or viruses), oil, heavy metals, and excess nutrients

Particles: sediment, plastic, debris, and other small objects; for simplicity, in this article we also use this term to refer broadly to all transported materials, including plankton and pollutants

Nearshore: the region within several kilometers of the coastline

The coastal ocean is used extensively for commerce and recreation, and more than 40% of Earth's population lives within 100 km of the coast (CIESIN 2012). Our ability to protect and enjoy this region relies on an understanding of how water, plankton, pollutants, particles, and other materials move from the coast to offshore and vice versa. Shellfishing and recreational beach use require accurate water quality information, as microbial and nutrient pollution at the coast threatens nearshore ecosystems (Boehm et al. 2017), swimming and recreation in contaminated nearshore waters can lead to gastrointestinal and viral infections (Prüss 1998, Colford et al. 2012), and harmful algal blooms originating offshore can threaten aquaculture. Management of fisheries and marine protected areas relies on understanding cross-shore exchange in coastal waters, as many marine species have larval stages whose movement to and from suitable coastal habitats is governed by ocean currents (Cowen & Sponaugle 2009, Pineda & Reyns 2018).

Particles moving to or from the coast transit through the surf zone and the inner part of the continental shelf. In this nearshore region (**Figure 1**; see also the sidebar titled Defining the Nearshore Region), the dynamics controlling circulation and exchange are largely distinct from the dynamics of deeper waters. Whereas cross-shore circulation in deeper waters is controlled primarily by along-shelf winds and along-shelf pressure gradients, cross-shore circulation in the nearshore is more strongly influenced by other processes, including cross-shore winds, surface and internal gravity waves, and surface heating and cooling (**Figure 1a**). The relative importance of these processes varies in space and time and depends on a variety of factors, including the presence and strength of winds, stratification, and surface and internal waves, along with the thickness of turbulent boundary layers (**Figure 1b**). In addition, the nature of the material being moved by these processes must be considered, as buoyant material, including oil or plastic, or sinking and swimming particles, such as sediment and larvae, may follow different transport pathways than dissolved chemicals or other neutrally buoyant material (**Figure 1b**).
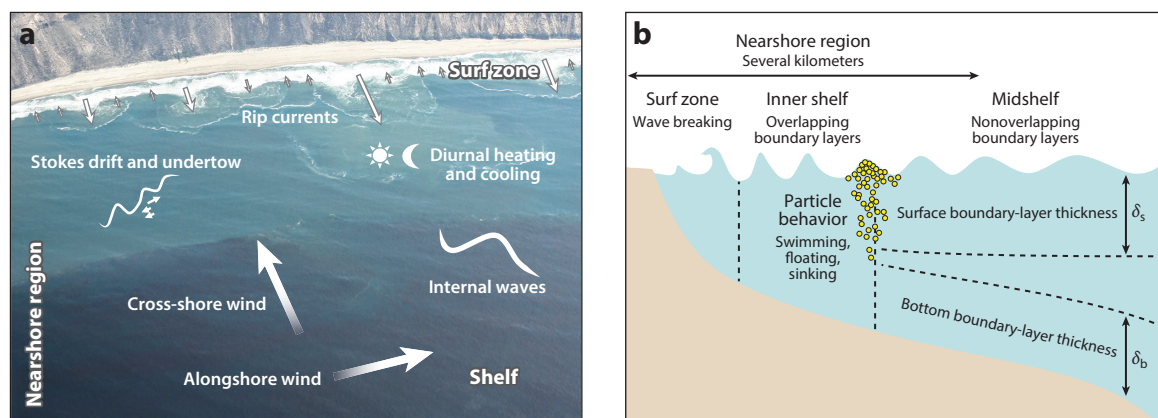

Figure 1

(*a*) Nearshore region on the central coast of California. Foam, sediment, and algae are being moved between the beach and the shelf by multiple processes. Aerial photo by M. Moulton and C.C. Chickadel. (*b*) Schematic of nearshore subregions and boundary layers.

DEFINING THE NEARSHORE REGION

The terms nearshore and inner shelf are used extensively by marine ecologists and oceanographers. The definitions of these terms, however, vary from one community to another and with the processes being studied. For coastal oceanographers and engineers who study surface gravity waves, the nearshore may refer to the surf and swash zones, where waves break and run up the beach. Those who study wind-driven circulation define an inner shelf, the region where turbulence extends throughout the water column, excluding the surf zone (Lentz & Fewings 2012). Others working on interdisciplinary coastal topics have defined the nearshore region to include wetlands; estuaries; dunes; beaches; the intertidal, swash, and surf zones; the innermost part of the shelf; and the built environment (Elko et al. 2015). In part because a fixed region is useful for monitoring programs with frequently sampled stations, marine ecologists sometimes define the nearshore as the region onshore of the ~30-m isobath (Grantham et al. 2004, Morgan et al. 2018b).

In this review, we define the nearshore as the region extending from the shoreline to a few kilometers offshore, which often encompasses several subregions with different dominant dynamics (**Figure 1b**). This review integrates across these subregions to describe how several processes drive the exchange of plankton, pollutants, and other material between the shoreline and the continental shelf.

In this review, the strength of cross-shore exchange driven by multiple processes is estimated in a consistent framework using a horizontal exchange velocity or diffusivity, depending on particle behavior and the distribution of turbulence in the water column. We quantify the strength of exchange due to each process based on background conditions and the strength of forcing at a given coastal location and time so that the relative importance of processes can be assessed. An underlying assumption is that a given stretch of coastline, and the exchange processes present, can be treated as locally alongshore uniform over several kilometers and statistically steady in time over hours or days. Even with that simplification, this framework allows for the assessment of how exchange due to multiple processes differs from one stretch of coastline to the next or from one time to another. As a given planter or particle crosses the shelf, it often also moves alongshore a substantial distance and thus may experience several regions and time periods with varying exchange.

This review focuses on simple theoretical metrics that describe the strength of a suite of nearshore exchange processes. Numerous observational studies provide an important foundation for the theory, but as no review can be exhaustive, the observational studies are not addressed in detail here, nor are exchange processes that lack simple parameterizations. We do not review the role of alongshore varying coastline topography, including eddies and submesoscale filaments or three-dimensional alongshore flows generated by wind relaxations or other flows near headlands, nor do we review exchange due to freshwater input from the coast and associated buoyant plumes, which are extensively covered elsewhere (Geyer & MacCready 2014, Horner-Devine et al. 2015, Brasseale & MacCready 2021).

2. CONSIDERING PARTICLE BEHAVIOR AND WATER COLUMN TURBULENCE IN CROSS-SHORE EXCHANGE

This review introduces a framework to estimate the relative importance of various physical processes to exchange across the nearshore. This framework is effectively a taxonomy of nearshore processes summarized by two flowcharts: one to determine how vertical behavior affects exchange (**Figure 2a**) and one to determine which cross-shore exchange processes are important at a given location and time (**Figure 2b**). This section details how to assess water column conditions and

Cross-shore exchange: the movement of material toward or away from the coast

a Particle vertical behavior resulting in horizontal exchange velocity or diffusivity
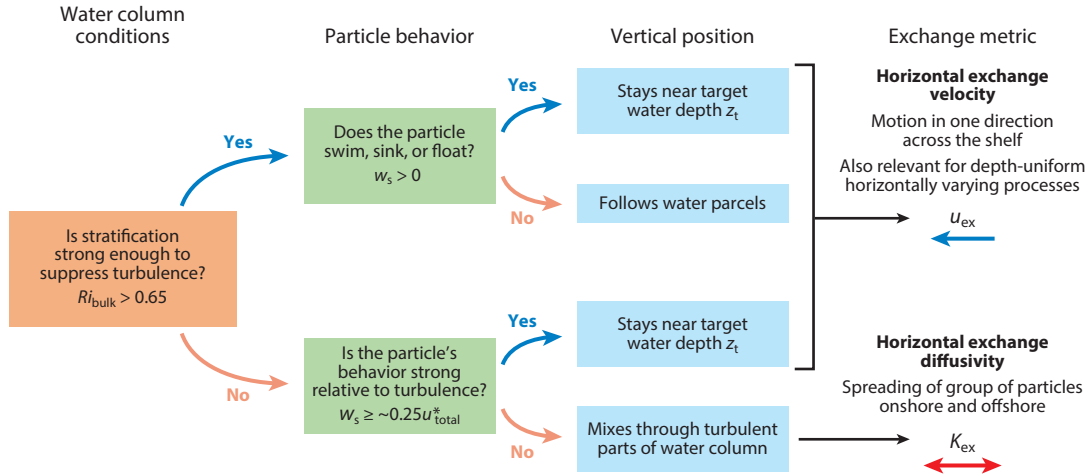
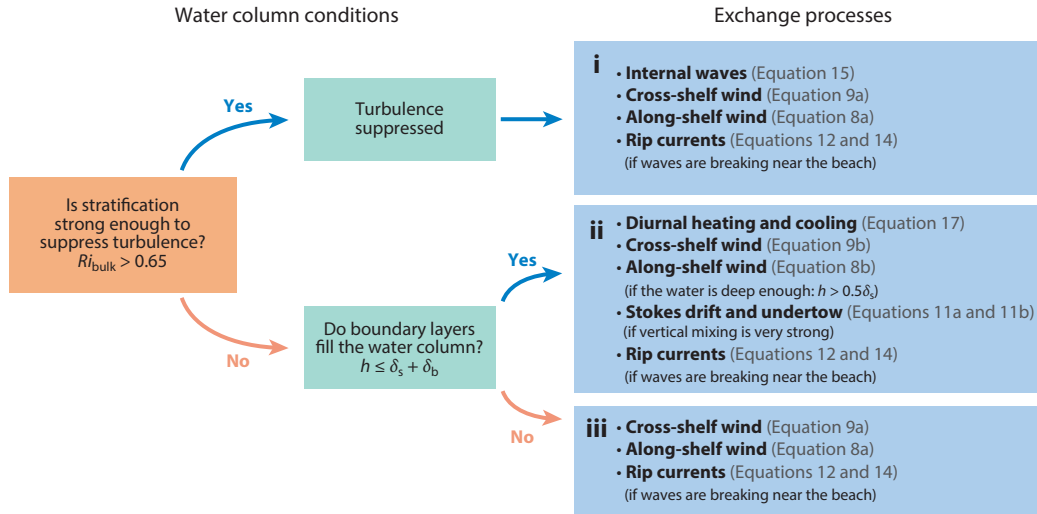**b** Relative importance of cross-shore exchange processes

Figure 2

Flowcharts to determine (*a*) the vertical position of a group of particles and the appropriate cross-shore exchange metric and (*b*) candidate physical processes likely to dominate exchange for a given location and time. In both panels, the first steps require characterizing the strength of the stratification and turbulence (see Sections 2.1 and 2.2 and the sidebar titled Sources of Turbulence in the Nearshore). In panel *a*, if the particles are mixed through the water column, then their onshore and offshore spreading rates are characterized by an exchange diffusivity (Section 2.4), whereas if the particles stay near a target depth, then they move at a rate characterized by an exchange velocity (Section 2.5; **Figure 3**). In panel *b*, different water column conditions lead to different candidate exchange processes in boxes *i*, *ii*, and *iii*, whose relative importance can be assessed with an exchange velocity (the relevant equations are shown in *gray*; see Sections 3–6).

particle behavior, which determine whether particles mix vertically and are spread both onshore and offshore at a rate described by an exchange diffusivity K_{ex} or hold a depth and move in one direction with a speed characterized by an exchange velocity u_{ex}. Subsequent sections describe how water column and forcing conditions control the strength of individual exchange processes,

each quantified with a process-specific u_{ex}. Section 7 presents an example using conditions representative of central California.

2.1. Is Stratification Strong Enough to Suppress Turbulence?

The first step in determining dominant exchange processes is to identify the state of the ocean at a point of interest (**Figure 2**). The vertical distribution of turbulence in the water column affects the magnitude of the exchange velocity driven by winds, waves, and other processes (see the sidebar titled Sources of Turbulence in the Nearshore). In addition, the interaction of turbulence with particle behavior affects the way particles move cross-shore. Our framework assumes that where water is stratified, turbulence is either weak or transient, as stratification tends to suppress turbulence, while turbulence maintained by sufficient forcing rapidly destroys stratification (Pollard et al. 1972, Price et al. 1986). More formally, shear-driven turbulence exists and rapidly mixes the water column when

$$Ri_{bulk} = \frac{g \Delta \rho h}{\rho_0 |\Delta \mathbf{u}|^2} \qquad \qquad 1.$$

is less than ~0.65 (Price et al. 1986), where Ri_{bulk} is the bulk Richardson number, $\Delta \mathbf{u}$ is the near-surface-to-near-bottom difference in the horizontal velocity vector $\mathbf{u} = (u, v)$, including contributions from both the cross-shelf component of velocity u and the along-shelf component of velocity v, and $\Delta \rho$ is the magnitude of the top-to-bottom density difference. Even when turbulence is caused by mechanisms other than shear, small values of Ri_{bulk} indicate an unstratified or weakly stratified water column, from either past or ongoing mixing.

Values of $Ri_{bulk} > 0.65$ indicate that, on average, the water column is stably stratified and turbulence is suppressed (box i in **Figure 2b**). If $Ri_{bulk} < 0.65$, then the dominant exchange processes depend on the turbulent boundary-layer thicknesses δ relative to the total water depth h, as detailed in Section 2.2 (Equation 2; see also the sidebar titled Sources of Turbulence in the Nearshore).

2.2. Do Boundary Layers Fill the Water Column?

If the water column is unstratified in the bulk Richardson number sense ($Ri_{bulk} > 0.65$; Section 2.1) and the depth is less than the Ekman depth, then turbulence extends through the water column and the surface and bottom boundary layers are merged. The Ekman depth is the distance that turbulent mixing allows surface and bottom stress to drive fluid motions, and in an unstratified ocean is (Madsen 1977)

$$\delta = \frac{\kappa u^*_{total}}{f}. \qquad \qquad 2.$$

The quantity u^*_{total} is the sum resulting from all sources of turbulence (see the sidebar titled Sources of Turbulence in the Nearshore). If the water column is stratified ($Ri_{bulk} > 0.65$), there are usually separate turbulent boundary layers near the surface and bottom of thickness δ_s and δ_b, respectively (**Figure 1b**). Turbulence and u^* are effectively zero in the stratified mid–water column. The thicknesses of the boundary layers are an active area of research; boundary layers can be thick even during periods of low winds or weak currents because the boundary-layer water was mixed by past winds, currents, and cooling events. Nonetheless, it is possible to estimate the minimum boundary-layer thickness, given an initial stratification with corresponding buoyancy frequency N.

Exchange diffusivity (K_{ex}): the rate at which particles spread horizontally due to being mixed vertically through both onshore and offshore flows

Exchange velocity (u_{ex}): an approximate scale for the time-mean cross-shore velocity toward or away from shore

Bulk Richardson number (Ri_{bulk}): a measure of water column instability and tendency to mix vertically

g: acceleration due to gravity

ρ_0: reference density of seawater

κ: von Kármán's constant (~0.4)

f: the Coriolis parameter (~10^{-4} s^{-1} at midlatitudes)

Buoyancy frequency (N): a measure of the strength of vertical density stratification; $N^2 = -\frac{g}{\rho_0} \frac{\partial \rho}{\partial z}$, and $N^2 \approx -\frac{g}{\rho_0} \frac{\Delta \rho}{h}$

SOURCES OF TURBULENCE IN THE NEARSHORE

There are several sources of turbulence in the nearshore. Wind stresses at the sea surface and frictional stresses at the seabed lead to vertically sheared (i.e., depth-varying) velocities that reduce water column stability and can cause turbulence. Stress is the exchange of momentum between layers in the ocean, the atmosphere above, and the bottom below. The bottom stress τ_b is driven by bottom currents and can be enhanced by surface waves and bottom ripples; its calculation and dynamics were reviewed by Trowbridge & Lentz (2018). The surface stress τ_s, caused primarily by winds, can be estimated from wind velocity using a bulk formula such as the Coupled Ocean–Atmosphere Response Experiment (COARE) algorithm (e.g., figure 3 in Edson et al. 2013). These stresses cause turbulent velocity fluctuations in the water column in turbulent surface and bottom boundary layers, which can be calculated as (Stull 1988)

$$u^* = \sqrt{\frac{|\tau_s|}{\rho_0}} \text{ and } \sqrt{\frac{|\tau_b|}{\rho_0}}$$

for the surface and bottom, respectively. Typically, u^* is approximately one-thousandth the wind speed, or 1 cm s^{-1} for a 10 m s^{-1} wind. The near-bottom turbulent velocity scale is typically similar.

Surface waves contribute to turbulence via several mechanisms. Langmuir cells, which result from the interaction of horizontal wind shear and wave-induced Stokes drift in a turbulent boundary layer, are counterrotating vortices at the ocean surface that can be visible as wind rows. These features enhance turbulence above that predicted by boundary-generated u^* (equation above) and in shallow water may increase turbulence throughout the water column (Li & Fox-Kemper 2017, Savidge & Gargett 2017). Wave breaking also enhances turbulence both for surf-zone breaking (Feddersen et al. 2007), which here is always assumed to be sufficient to mix the water column, and for whitecapping (Terray et al. 1996).

Internal waves also may increase turbulence, particularly at the leading edge of nonlinear internal waves shoaling toward the coast (MacKinnon & Gregg 2005, Walter et al. 2014, Becherer et al. 2020). Surface cooling can drive convection and turbulence, with magnitude w^* (this is customary notation and is not meant to suggest a vertical velocity) depending on the surface heat flux Q and scaling as (Stull 1988)

$$w^* = \left(\frac{\alpha_T g h Q}{\rho_0 c_p}\right)^{1/3},$$

where α_T and c_p are the thermal expansion coefficient and specific heat capacity of seawater, and h is the depth of the surface mixed layer, or the water depth if the turbulence extends through the water column.

All of these sources are combined into u^*_{total}, the sum of all sources of turbulent fluctuations, including shear (u^*), surface cooling (w^*), and the other sources of turbulence.

Ekman transport:
volume transport of $|\tau_s|/(\rho_0 f)$ per meter of along-wind direction (90° to the right of the wind in the Northern Hemisphere)

The minimum thicknesses of the bottom and surface boundary layers were quantified by Weatherly & Martin (1978) and Pollard et al. (1972), respectively. Both solutions assume that the wind or currents set up Ekman transports and thicken the boundary layer until Ri_{bulk} is large enough that the stratified water no longer mixes. Within a day, the boundary layer grows to a thickness of

$$\delta = C u^* (Nf)^{-1/2}. \qquad \qquad 3.$$

For the surface boundary-layer thickness δ_s, u^* is the u^* driven by surface wind stress, and for the bottom boundary layer δ_b, it is the u^* associated with bottom stress resulting from mean alongshore and cross-shore currents and waves (see the sidebar titled Sources of Turbulence in the Nearshore). C is a constant that ranges from approximately 1.3 to 1.7. Note that these results neglect additional

mixing caused by surface gravity waves and cooling (Price et al. 1986) and the role of bottom slope (Brink & Lentz 2009). If $\delta_s + \delta_b$ exceeds the water depth, then the water column is unstratified or weakly stratified.

2.3. Particle Behavior and Turbulence: Vertically Mixed or Target Depth?

Ocean currents are often described by the time-average velocity at a point. However, the displacement of a parcel of water or a particle, be it a plankter or a molecule of nutrient or pollutant, is governed not only by that time-mean flow but also by Stokes drift (Sections 4.1 and 5.2) and the sum of the turbulent velocity fluctuations the particle encounters. Consider a group of particles in a water column forced by an onshore wind, which drives both a two-layer downwelling circulation and turbulence extending through the water column. If particles initially near the surface do not feel the effects of the turbulence, either because the turbulence is weak or because the particles' behavior or buoyancy keeps them from being dispersed vertically by the turbulence, then they follow the time-mean current and are swept toward the shore at the surface. If a large number of particles are released together, then they remain near the surface and move onshore together until they are trapped near the coast (**Figure 3c**).

If, on the other hand, the particles released near the surface have insufficient depth-keeping behavior (**Figure 3a**), then they are mixed vertically throughout the water column by the turbulence. The turbulence brings particles near both the surface, where they temporarily experience an onshore motion, and the bottom, where they temporarily experience an offshore motion. The net cross-shore motion of any particle is small, and as a group, the particles do not move onshore on average (the mean position of the yellow dots in **Figure 3a** does not change in time). Instead, the overall motion appears as a diffusion of the particles, with the cloud of particles expanding in time in both the offshore and onshore directions (Bowden 1965). These two potential particle pathways are very different: One is a near-steady cross-shelf motion of particles that remain near the surface, and the other is a random walk onshore and offshore of particles that are mixed vertically.

The ability of the particles to maintain their depth by swimming or buoyancy can be compared with the tendency of turbulence to disperse the particles vertically by comparing the total turbulent velocity scale u^*_{total} with a particle's swimming, sinking, or floating speed w_s. If a particle can sink or swim at a speed comparable to or greater than the turbulent velocities ($w_s > 0.25u^*_{total}$), then the depth of the particle is determined largely by its own behavior and not by the vertical turbulent mixing, and the particle moves with the mean velocity at its target depth (Fredsoe & Deigaard 1992, Pringle & Franks 2001) (**Figure 3d**). The motion of weakly swimming particles may also be described by an exchange velocity in the case where the particles are mixed over a near-surface turbulent boundary layer but are not mixed down into a stratified mid–water column (not shown); these particles thus experience horizontal flow in only one direction.

However, the turbulent velocity u^*_{total} ($\sim$1 cm s^{-1}) is often large relative to swimming or sinking speeds, and in the case of dissolved molecules (e.g., dissolved pollutants or other tracers), this is always true. Vertical mixing dominates when $w_s/u^*_{total} < 0.25$ and the particles are mixed vertically between the surface and bottom in turbulent and unstratified waters (**Figure 3d**).

When the particle swimming or depth-seeking speed is intermediate to the two cases discussed above ($w_s/u^*_{total} \approx 0.25$), a combination of mean cross-shelf motion and horizontal diffusion occurs (**Figure 3b**). Particles on average are moved in the direction of the mean currents at the depth they seek but still experience some horizontal dispersal around that point.

Note that when cross-shore currents are approximately depth uniform, such as in rip currents and surf-zone eddies, a particle's vertical position has little effect on its cross-shore motion, and the exchange velocity is always the appropriate metric.
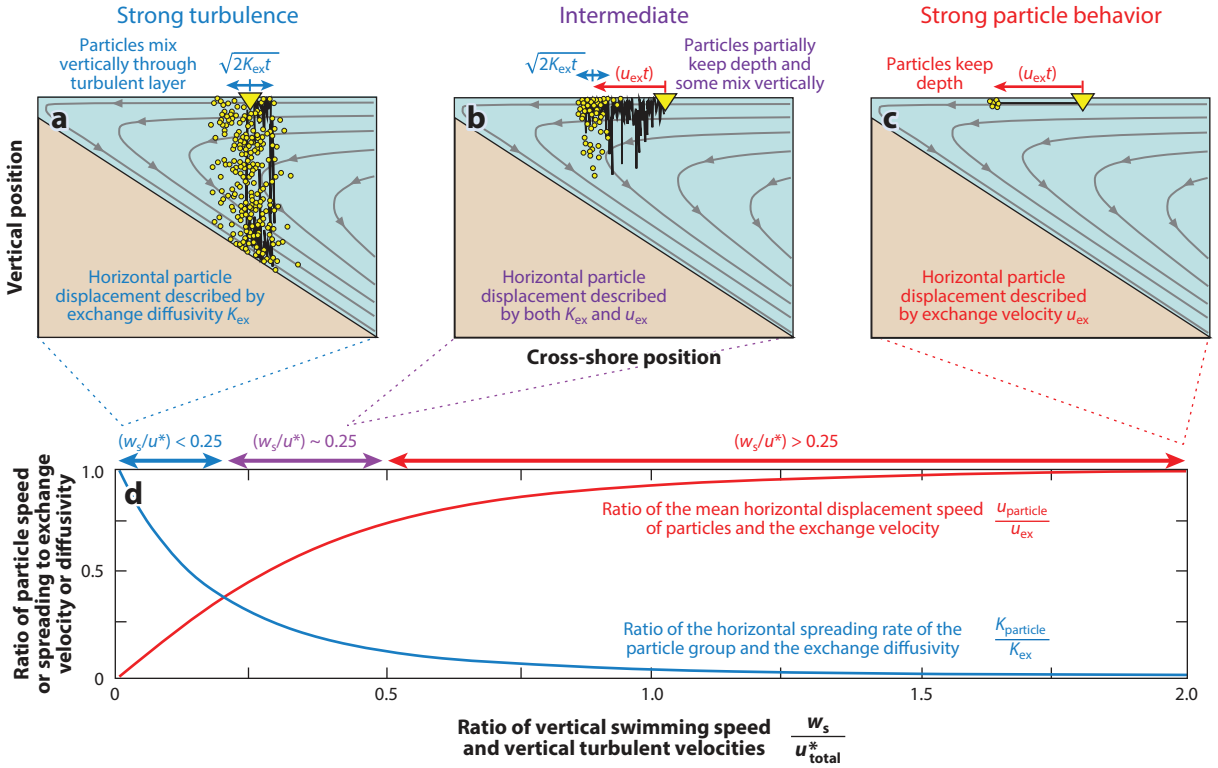
Figure 3

(*a–c*) Simulated movement of particles with variable swimming behavior across the shelf over 0.6 days in a downwelling circulation (*gray streamlines*) in an unstratified, turbulent nearshore. Particles start at the yellow triangle and have swimming speeds much less than the turbulent velocities ($w_s \ll u^*$) (panel *a*), comparable to the turbulent velocities ($w_s \approx 0.4u^*$) (panel *b*), or larger than the turbulent velocities ($w_s \approx 2u^*$) (panel *c*). (*d*) The ratio of cross-shore particle diffusivity (related to the spreading rate of the simulated particles) $K_{particle}$ and exchange diffusivity K_{ex} (*blue curve*) and the ratio of mean cross-shore particle speed $u_{particle}$ and exchange velocity u_{ex} (*red curve*) plotted as functions of the ratio of vertical particle speed and turbulent velocity scale w_s/u^*_{total}. When $w_s/u^*_{total} > 0.25$, the effect of vertical particle behavior dominates. In all panels, the flushing time for the area inshore of the release point is 2.5 days, u^* is 0.005 m s^{-1}, and the near-surface and near-bottom cross-shelf velocities are $5u^*$. For assumptions about the vertical profiles of circulation and diffusivity, see Section 2.4. Code to reproduce or modify this figure and the underlying analysis is available at **https://doi.org/10.5281/zenodo.6812919** (Pringle 2022).

2.4. Vertically Mixed: Horizontal Exchange Diffusivity

In the case of weak depth keeping, the magnitude of the horizontal cross-shelf exchange diffusivity of a group of particles (**Figure 3**) is a function of the strength of the horizontal circulation and vertical turbulence. Assuming a profile of cross-shelf velocity that goes linearly from $-2u_{ex}$ at the bottom to $2u_{ex}$ at the surface (similar to, e.g., the flow forced by cross-shelf wind; Lentz & Fewings 2012) and a turbulent vertical mixing profile that is a quadratic function of depth, with a slope κu^*_{total} at the top and bottom [suggested as a reasonable choice by Lentz (1995) and references therein], the approach of Bowden (1965) can be used to calculate an effective horizontal exchange diffusivity of

$$K_{ex} = \frac{2u_{ex}^2 h}{3\kappa u^*}. \qquad 4.$$

The typical distance a particle moves from its starting point in time t can be approximated by the standard deviation of the distances that individual particles in the cloud move: $\sqrt{2K_{ex}t}$ (**Figure 3a**).

2.5. Target Depth or Depth-Uniform Flows: Horizontal Exchange Velocity

Cross-shelf exchange can be quantified using an exchange velocity, an approximate scale for the time-mean cross-shore velocity toward or away from shore. This velocity scale is relevant for particles that approximately keep their depth.

On relatively alongshore-uniform coastlines, onshore and offshore flows due to processes such as winds and internal waves are balanced over the water column (e.g., an offshore flow at depth balances an onshore flow at the surface). For these processes, the exchange velocity can be defined as the vertical average of the magnitude of the cross-shore velocity from the surface to the depth where horizontal velocities first reverse, i.e., the first zero crossing z_c (**Figure 4a**) (similar to the definition of surface-layer transport in Lentz & Fewings 2012):

$$u_{ex}(x,y) = \frac{1}{h_c} \int_{z_c}^{0} |u(x,y,z)|\,dz, \qquad 5.$$

where x, y, and z are the cross-shore, alongshore, and vertical coordinates, respectively, and h_c is the thickness of the layer above the zero crossing (i.e., $h_c = -z_c$). For processes with multiple zero crossings, the depth integral can be defined to include all layers in which water is moving in one direction. The position of the sea surface, ignoring passing surface waves but including variations in the water column height due to atmospheric effects, tides, or other processes with timescales of hours and longer, is defined to be $z = 0$, with z positive upward. The cross-shore velocity u used to compute u_{ex} is the average velocity over turbulent fluctuations and surface waves, but may include variations on tidal, diurnal, or weather timescales. When computing an exchange velocity from
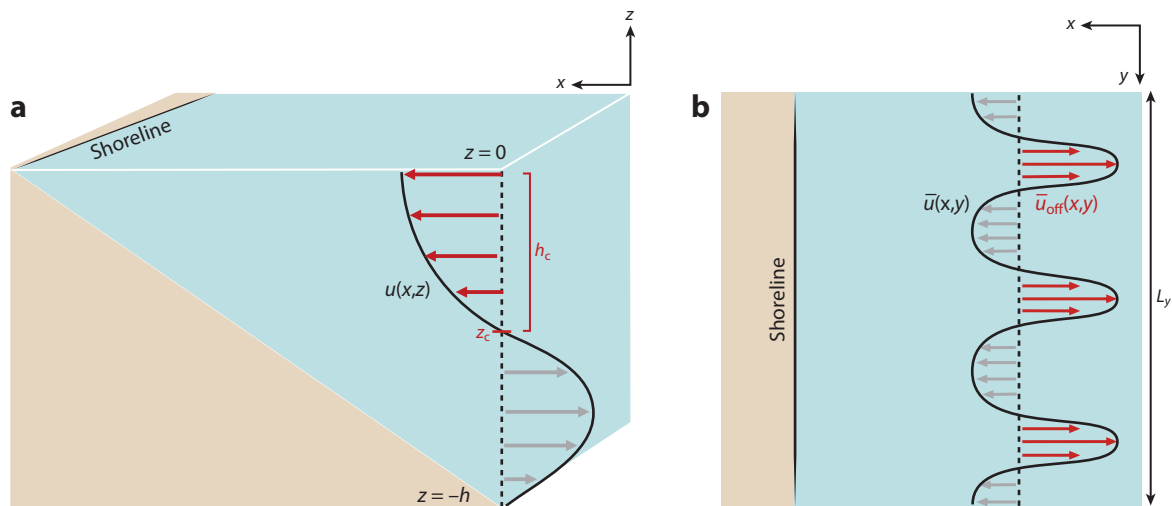

Figure 4

Schematic definition of exchange velocity for (*a*) vertically varying currents with an overturning pattern, for which u_{ex} is estimated by averaging the cross-shore velocity from the first zero crossing ($z = z_c$) to the surface (*red arrows*; Equation 5), and (*b*) horizontally varying depth-uniform processes, such as rip currents, for which u_{ex} is obtained by averaging the offshore-directed component of velocity (*red arrows*) along an alongshore length L_y (Equation 6). In both cases, the onshore and offshore transports balance.

observed cross-shelf velocities, if the depth-mean velocity is not near zero, it is sometimes removed before computing the exchange velocity, under the assumption that the depth-mean flow is caused by three-dimensional (alongshore-varying) dynamics not addressed here (Lentz & Fewings 2012).

For nearly depth-uniform circulations, such as rip currents, the water flowing offshore at one alongshore location is replaced by onshore-flowing waters at another location. Then, the exchange velocity is defined as the alongshore average of the offshore-directed component of the depth-averaged flow, $\bar{u}_{off}$ (red arrows in **Figure 4b**) (Suanda & Feddersen 2015):

$$\bar{u}_{ex}(x,y) = \frac{1}{L_y} \int_{y_0}^{y_0+L_y} |\bar{u}_{off}(x,y)| dy, \qquad 6.$$

where $\bar{u}_{off}(x,y) \equiv \bar{u}(x,y)$ when $\bar{u}$ is directed offshore and $\bar{u}_{off}(x,y) \equiv 0$ otherwise. This offshore-directed flow is averaged in the alongshore direction over a length of coastline $L_y \approx 1$ km, long enough to include multiple cross-shore flow features but short relative to the scale over which the surface wave field, winds, or sandbar patterns change.

These exchange velocities (Equations 5 and 6) differ to accommodate processes with different spatial structures. For example, when defining the exchange velocity for rip currents, we seek a speed representative of the mean experienced by particles with random horizontal positions, as plankton and other particles typically cannot control their horizontal position. By contrast, for vertically varying processes, an average magnitude within a particular layer is more relevant, as particles may stay at a target depth. These choices prevent a precise comparison of exchange magnitudes by different types of processes. However, both of these definitions provide a reasonable approximate magnitude for the flow that replaces the water near the coast with water from farther offshore, allowing for assessment of which processes are important or not. The exchange velocity definitions provided here have been used widely, but other definitions, including a depth- or alongshore-averaged magnitude of the cross-shore velocity, may have advantages for a given application.

The flushing time to replace all the water inshore of some cross-shore location is

$$T_{flush} = \frac{A_c(x)}{h_c(x)u_{ex}(x)}, \qquad 7.$$

where A_c is the cross-sectional area (in the x–z plane) of the nearshore region onshore of x, and h_c is the depth of the zero crossing, or the full water depth for depth-uniform processes.

3. WIND-DRIVEN EXCHANGE

3.1. Effect of Overlapping Boundary Layers

The water volume transport driven by wind differs depending on whether the surface and bottom turbulent boundary layers overlap to fill the water column with active turbulence (Lentz & Fewings 2012) (**Figure 1b**). If the surface and bottom turbulent boundary layers are separated by a less turbulent middle region, then Ekman transport can fully develop, and midshelf dynamics dominate (sensu Brink 2016). If the boundary layers fill the water column, then vertical mixing of momentum in the overlapping boundary layers weakens the wind-driven, cross-shelf volume transport compared with a case with nonoverlapping boundary layers (Austin & Lentz 2002), and inner-shelf dynamics dominate (sensu Lentz & Fewings 2012). Inner-shelf dynamics dominate from the edge of the surf zone to the location where the boundary layers no longer overlap (**Figure 1b**). Although the responses of volume transport differ between areas of overlapping and nonoverlapping boundary layers (**Figure 5**), the following subsections show that the exchange
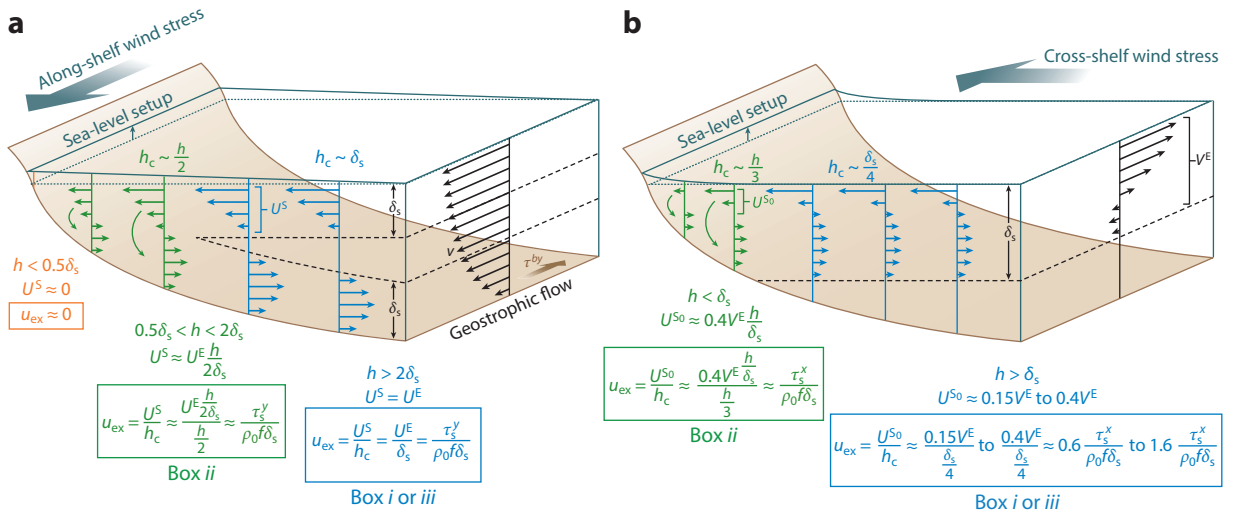
Figure 5

Cross-shelf exchange by (*a*) along-shelf and (*b*) cross-shelf wind stress, with boundary layers (*dashed lines*) and boxes in **Figure 2*b*** indicated. Figure adapted from Lentz & Fewings (2012).

velocities due to wind (Equations 8 and 9 below) do not depend as strongly on water depth as do the volume transports.

At any coastal location, the offshore extent of the region where the boundary layers overlap varies in time as wind forcing, bottom currents, and stratification change (Section 2.2). Boundary-layer thicknesses can be estimated as described in Section 2.2 and the sidebar titled Sources of Turbulence in the Nearshore. If the sum of δ_s and δ_b is less than the water depth, refer to Section 3.2; otherwise, refer to Section 3.3. The equations for wind-driven exchange velocity in the various cases are collected below for convenience and explained in the subsequent subsections:

$$
u_{ex}^{\text{wind, along-shelf}} \approx \begin{cases} \dfrac{\tau_s^y}{\rho_0 f \delta_s}, & \text{if } h > \delta_s + \delta_b & \text{(nonoverlapping boundary layers)} & 8a. \\[2ex] \dfrac{\tau_s^y}{\rho_0 f \delta_s}, & \text{if } 0.5\delta_s < h < 2\delta_s \text{ (or } \delta_s + \delta_b) & \text{(overlapping boundary layers),} & 8b. \\[2ex] 0, & \text{if } h < 0.5\delta_s & \text{(very shallow),} & 8c. \end{cases}
$$

$$
u_{ex}^{\text{wind, cross-shelf}} \approx \begin{cases} B\dfrac{\tau_s^x}{\rho_0 f \delta_s}, & \text{if } h > \delta_s \text{ (nonoverlapping boundary layers; coefficient } B \text{ varies} \\ & \qquad\qquad \text{from 1.6 to 0.6 for weak to strong stratification),} & 9a. \\[2ex] 1.2\dfrac{\tau_s^x}{\rho_0 f \delta_s}, & \text{if } h < \delta_s \text{ (overlapping boundary layers).} & 9b. \end{cases}
$$

3.2. Nonoverlapping Boundary Layers

3.2.1. Unstratified exchange driven by along-shelf wind.
An extensive body of literature describes the cross-shelf circulation that results from along-shelf wind forcing in the region where the water is deep enough or stratified enough that the surface and bottom turbulent boundary

layers do not overlap ($\delta_s + \delta_b < h$) (sensu Brink 2016). The simplest response to along-shelf wind forcing with nonoverlapping boundary layers occurs under restrictive assumptions: Water density is constant everywhere; there are no along-shelf variations in coastline shape or any other quantities; and the wind is uniform in space, is constant in time, and has been blowing long enough for the circulation to reach a steady state. This simple scenario is the canonical result with which more complicated scenarios are compared. The resulting steady cross-shelf circulation at midshelf has two key features (blue arrows in **Figure 5a**):

1. A surface turbulent boundary layer carries a cross-shelf transport of water volume U^S that is equal to the full theoretical Ekman transport value—i.e., $U^S = U^E \equiv \tau_s^y/(\rho_0 f)$, where τ_s^y is the along-shelf component of the wind stress. This volume transport does not depend on the surface-layer thickness. The associated exchange velocity scale u_{ex} (Equation 5), however, is the volume transport divided by the layer thickness: U^S/δ_s (Equation 8a), with δ_s estimated using Equation 2 and approaches to estimate stresses detailed in the sidebar titled Sources of Turbulence in the Nearshore. This flow is directed offshore at the surface for upwelling-favorable along-shelf winds and onshore at the surface for downwelling-favorable winds.

2. There is a compensating return transport lower in the water column that carries an equal volume of water in the opposite direction. In unstratified conditions, this return flow at mid-shelf occurs in a turbulent bottom boundary layer (Brink 2016), with transport equal and opposite to U^S. In this simple unstratified, steady scenario, the boundary-layer thickness and, therefore, the exchange velocity computed near the surface (Equation 5) are approximately equal to what they would be if they were computed near the bottom.

3.2.2. Stratified exchange driven by along-shelf wind.
Stratification complicates the possible scenarios substantially. In the relatively shallow nearshore, if the wind stress is strong, then the stratification is likely weak, as wind-driven vertical mixing destroys stratification, especially in the case of downwelling-favorable winds (Austin & Lentz 2002). Therefore, wind-driven exchange with strongly stratified dynamics is likely important in the nearshore only if the wind direction is upwelling-favorable and the wind is light.

In stratified conditions, the offshore-directed exchange velocity in the surface boundary layer can be estimated as in Section 3.2.1, using Equation 8, but estimating the surface boundary-layer thickness δ_s from Equation 3. Estimating the cross-shelf velocity in the lower water column during stratified upwelling is less straightforward. In the presence of strong vertical density stratification or a steeply sloping shelf, the return flow during upwelling may not be in a turbulent bottom boundary layer but can instead occur higher in the water column, including immediately below the surface boundary layer (Lentz & Chapman 2004, McCabe et al. 2015). In relatively shallow water, these effects are often assumed to be minor, in which case a cross-shelf exchange velocity computed over a bottom layer would be similar to the cross-shelf exchange velocity computed for the surface layer (Equation 5). If this assumption does not hold and return transport occurs over a thick interior layer instead of in a turbulent bottom boundary layer, the return velocity below the surface layer may be much weaker.

3.2.3. Exchange driven by cross-shelf wind.
In a turbulent surface boundary layer not in contact with the bottom, the total cross-shelf volume transport driven by the cross-shelf wind is zero. However, a nonzero cross-shelf velocity profile can exist within that layer (Tilburg 2003) (blue arrows in **Figure 5b**). Because water parcels are mixed vertically through the surface boundary layer, weakly swimming or neutrally buoyant organisms ($w_s/u^*_{total} < 0.25$) experience the diffusive scenario in Section 2.4. By contrast, depth-keeping, buoyant, or strongly upward-swimming organisms could experience a substantial cross-shelf exchange velocity near the surface in the

direction of the cross-shelf wind. Models indicate that the zero-crossing depth is approximately one-quarter the depth of the surface boundary-layer thickness, $h_c \approx \delta_s/4$ (Tilburg 2003, Estrade et al. 2008). If a cross-shelf wind blows over an unstratified water column, then the modeled transport above the zero-crossing depth is $U^{S_0} \approx 0.4V^E$, where $V^E = \tau_s^x/\rho_0 f$, the Ekman transport that would be driven to the right of the same wind in an offshore region of nonoverlapping boundary layers (blue in **Figure 5b**), resulting in an exchange velocity of $u_{ex} = U^{S_0}/h_c \approx 0.4V^E/(\delta_s/4) = 1.6V^E/\delta_s$ (Equation 9a). If a cross-shelf wind blows over a moderately or strongly stratified water column, then because the surface boundary layer is thinner than in the unstratified case (Section 2.2), the vertical shear that can exist in the cross-shelf velocity profile within that boundary layer is reduced, so the volume transport above the zero-crossing depth h_c is reduced (Tilburg 2003, Lentz & Fewings 2012). For example, for midlatitudes, numerical models show that when the interior stratification corresponds to $N^2 = 10^{-5}$ s^{-2}, then $U^{S_0} \approx 0.3V^E$ and $u_{ex} = 1.2V^E/\delta_s$ (Equation 9a) (Tilburg 2003). When the interior stratification corresponds to 10^{-3} s^{-2}, then $U^{S_0} \approx 0.15V^E$ and $u_{ex} = 0.6V^E/\delta_s$. To estimate δ_s, use Equation 2 for unstratified conditions ($Ri_{bulk} < 0.65$; Equation 1) and Equation 3 for stratified conditions ($Ri_{bulk} > 0.65$). Note that the u_{ex} estimated here represents only the near-surface exchange velocity. If a return exchange velocity were defined for the lower part of the surface boundary layer, it would be weaker by a factor of $\sim$3 due to a thicker sublayer (offshore-directed blue arrows in **Figure 5b**).

3.3. Overlapping Boundary Layers

3.3.1. Unstratified exchange. Where surface and bottom boundary layers overlap, cross-shelf winds are more effective than along-shelf winds at driving cross-shelf transport (Lentz & Fewings 2012). This is because the Coriolis effect, which is necessary for along-shelf winds to drive cross-shelf transport, becomes negligible as the timescale for mixing water parcels and momentum vertically is short compared with the timescale of Earth's rotation. As a result, the cross-shelf circulation driven by along-shelf wind weakens, allowing transport driven by cross-shelf winds to dominate in shallow water (Tilburg 2003).

Transport and exchange driven by the along-shelf wind in a region of overlapping boundary layers can be understood as a partially developed version of the midshelf scenario in Section 3.2 (Lentz & Fewings 2012). The fraction of the midshelf transport that develops in response to along-shelf wind forcing depends on the extent of boundary-layer overlap or, equivalently, the strength of vertical mixing or the water depth relative to the boundary-layer thicknesses. Where the boundary layers overlap, U^S decreases with decreasing water depth (sensu Lentz & Fewings 2012). The depth of the zero crossing of the cross-shelf velocity profile h_c also decreases with water depth, however, so the two effects compensate when estimating exchange velocity. Therefore, where boundary layers overlap, the exchange velocity scale $u_{ex} = U^S/h_c$ (Equation 5) does not decrease with water depth in the same manner as the volume transport U^S. If the boundary layers are only somewhat overlapping, then the exchange velocity is similar to the case of nonoverlapping boundary layers (Equation 8b; green in **Figure 5a**). Only where the water is very shallow compared with the boundary-layer thickness ($h < 0.5\delta_s$) does the exchange velocity associated with along-shelf wind approach zero (Equation 8c; red in **Figure 5a**).

Transport and exchange driven by the cross-shelf wind where the boundary layers fill the water column result from different dynamics than exchange driven by the along-shelf wind (Lentz & Fewings 2012). However, it is still convenient to measure volume transport relative to V^E. As reviewed by Lentz & Fewings (2012), in the region where turbulent boundary layers fill the entire water column, models (Tilburg 2003, Estrade et al. 2008) and observations (Fewings et al. 2008) indicate that the zero-crossing depth is approximately one-third of the water depth, $h_c \approx h/3$

(green in **Figure 5b**) and that the transport above this depth is $U^{S_0} \approx 0.4 V^E h / \delta_s$, resulting in a somewhat reduced exchange velocity due to cross-shelf wind (Equation 9b).

3.3.2. Weakly stratified exchange with overlapping boundary layers.

Although our framework assumes that boundary-layer mixing and strong stratification do not coexist, there can be weak stratification where boundary layers overlap. Even weak vertical density stratification increases the effectiveness of wind in driving cross-shelf exchange, as any nonzero stratification reduces the boundary-layer thicknesses and overlap associated with a given wind stress (Section 2.2), thereby increasing exchange. For instance, weak stratification can be maintained in a region of overlapping boundary layers by an upwelling-favorable, along-shelf wind importing denser, more stratified water toward the coast (Austin & Lentz 2002) or by straining of a cross-shelf density gradient (Horwitz & Lentz 2014, 2016) (not shown in **Figure 5**). Because typical wind stresses are a combination of along- and cross-shelf components, straining causes the response to cross-shelf wind to depend on the direction of the along-shelf wind component and vice versa. Estimating how much the exchange is enhanced requires a measurement of the cross-shelf density gradient (Horwitz & Lentz 2014, 2016). Near the outer edge of the surf zone, waters can transition from being unstratified to stratified; the resulting cross-shelf density gradients may also modify the response to wind, but it is unclear whether the effect is similar to the dynamics described by Horwitz & Lentz (2014, 2016).

4. SURFACE WAVE PROCESSES

Surface gravity waves contribute to multiple processes that drive cross-shelf transport of material in the nearshore, including Stokes drift, undertow, and rip currents (Lentz & Fewings 2012, Morgan et al. 2018b). Surface waves include locally generated wind waves and waves generated at a distance that arrive as swell. The wave field includes a range of heights, periods, and directions and can be described by a frequency-directional spectrum or, more simply, by bulk parameters that summarize the spectrum: significant wave height H_s, peak period T_p, mean direction θ (propagating from and measured relative to shore-normal), and directional spread σ_θ.

As waves propagate into shallower water, they refract, steepen, and break. This wave breaking, referred to as depth-limited wave breaking to distinguish it from wind-driven whitecapping, occurs approximately when the wave height first exceeds a fraction of the water depth γ, such that the significant wave height at breaking is $H_{s,br} = \gamma h_{sz}$. The value of γ varies for different beaches and wave conditions but is typically $\sim$0.3–0.8 (Battjes & Janssen 1978). The depth h_{sz} where waves start breaking defines the outer edge of the surf zone, at a distance L_{sz} from shore known as the surf-zone width. When breaking occurs, there is a gradient in the momentum flux associated with waves, which may drive water-level setup and circulation (Longuet-Higgins & Stewart 1964, Lentz & Raubenheimer 1999, Raubenheimer et al. 2001). Nearshore circulation, including longshore currents and rip currents, impacts the dispersal of larvae and other material near the beach (Rilov et al. 2008, Morgan et al. 2018b).

4.1. Stokes Drift and Undertow

Stokes drift is the net drift velocity in the direction of wave propagation that results because the orbits of particles moving with wave motions are not closed (van den Bremer & Breivik 2017, Monismith 2019). Wave orbital velocities are typically one to several meters per second, whereas the resulting Stokes drift is typically several centimeters per second. Stokes drift is accompanied by an opposing return current referred to in the coastal ocean as undertow (sensu Lentz & Fewings 2012), and the net contribution of Stokes drift and undertow to exchange strongly depends on vertical turbulent mixing.
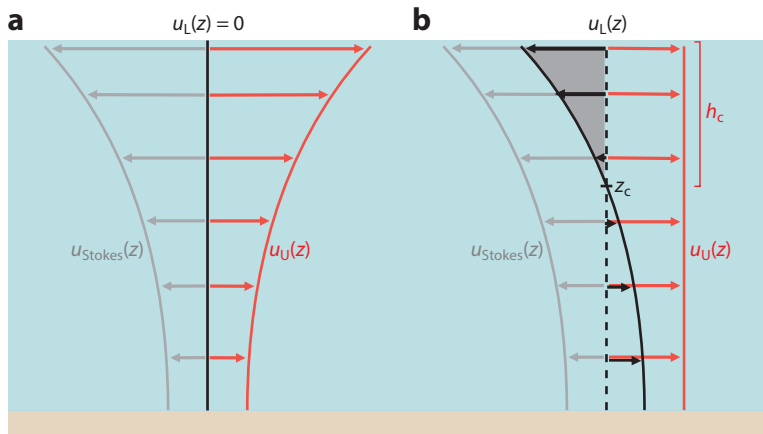
Figure 6

Schematic of Stokes drift (*gray arrows*), undertow (*red arrows*), and net Lagrangian circulation (*black lines and arrows*) profiles for (*a*) weak and (*b*) strong mixing cases, with waves propagating to the left. The area of the gray shaded region in panel *b* is $u_{ex}^{Stokes} h_c$.

The magnitude of surface wave Stokes drift is maximum at the surface, decaying vertically with a scale proportional to the wavelength (**Figure 6**). The total Stokes drift can be computed by integrating contributions over frequency and direction (Kumar et al. 2017), but an estimate based on a single set of bulk wave parameters is usually within a factor of two, sufficiently accurate for estimating an approximate magnitude of exchange. The cross-shore component of the Stokes drift velocity is

$$u_{\text{Stokes}}(z) = \frac{1}{16} H_s^2 \omega k \cos(\theta) \frac{\cosh\left[2k(z+b)\right]}{\sinh^2 kb}.$$ 10.

On a straight coast, there is zero net mass flux at the coastal boundary because water cannot flow through the coast, and an offshore-directed undertow u_U compensates the mass flux by Stokes drift, such that $\int_{-b}^{0} u_U(z)\mathrm{d}z = -\int_{-b}^{0} u_{\text{Stokes}}(z)\mathrm{d}z$. While the total mass fluxes integrated over depth balance, the Stokes drift and undertow may have different vertical profiles and thus may result in a net Lagrangian overturning circulation, $u_L(z) = u_{\text{Stokes}}(z) + u_U(z)$ (black lines and arrows in **Figure 6**). The exchange velocity associated with Stokes drift and undertow is estimated by integrating this Lagrangian velocity to the first zero crossing, as in Equation 5: $u_{ex}^{\text{Stokes}} = \frac{1}{b_c} \int_{z_c}^{0} u_L(z)\mathrm{d}z$. Note that in the surf zone, additional wave-driven mass fluxes associated with nonlinear effects and wave breaking may be of a similar size to the Stokes drift (Garcez Faria et al. 2000); thus, the exchange velocity presented here could underestimate the exchange resulting from waves.

The undertow profile and resulting net Lagrangian circulation depend on the strength of vertical mixing. In and near the surf zone, where vertical mixing is strong, undertow can be approximately vertically uniform (Lentz et al. 2008) (**Figure 6b**); a parabolic undertow profile has also been observed, which leads to similar exchange estimates. By contrast, where mixing is weaker, a return current with a vertical profile equal and opposite to the Stokes drift is thought to result from an interaction of the surface waves with Earth's rotation, the Stokes–Coriolis force (Hasselmann et al. 1973) (**Figure 6a**). An additional return current is predicted to result from Stokes drift interacting with turbulence, even without rotation (Pearson 2018), but is not included here. The Stokes–Coriolis return current balances the Stokes drift at each vertical level, yielding a Lagrangian transport of zero at each vertical level. Thus, there is no net exchange, and u_{ex}^{Stokes} is zero. Somewhat surprisingly, even observations and models on the inner shelf with relatively

$\boldsymbol{\omega}$: angular frequency; $\omega = 2\pi/T_p$, and for surface waves, $\omega^2 = gk\tanh(kb)$

$\boldsymbol{k}$: wavenumber; $k = 2\pi/\lambda$, where λ is the wavelength

strong mixing ($h < \delta_{s} + \delta_{b}$) appear to be consistent with this theory (Lentz et al. 2008, Kirincich et al. 2009, Lentz & Fewings 2012). Yet others have suggested that net exchange due to surface waves may occur under a broader range of conditions (Clarke & Van Gorder 2018), especially very near the surface, a region that is difficult to observe or model accurately.

The location of the transition between these stronger and moderate-to-weak mixing cases is not well established, but it may occur where h is no longer much less than $\delta_{s} + \delta_{b}$ (Lentz et al. 2008). Alternatively, proximity to the surf zone may be important, with a transition perhaps several surf-zone widths from shore or at a depth several times the depth at the outer edge of the surf zone (Kumar et al. 2017). These assumptions result in the following estimate for the exchange velocity for Stokes drift and undertow:

$$
u_{\text{ex}}^{\text{Stokes}} \approx
\begin{cases}
0, & \text{if } h > 0.1(\delta_{s} + \delta_{b}) \text{ (weak to moderate mixing)}, & \text{11a.} \\
0.61 \frac{1}{16} H_{s}^{2} \omega k \cos(\theta), & \text{if } h < 0.1(\delta_{s} + \delta_{b}) \text{ (very strong mixing)}. & \text{11b.}
\end{cases}
$$

Note that the approximations leading to Equation 11b apply well for $kh < 5$, which is almost always the case for the wave conditions of interest here, particularly given $h < 0.1(\delta_{s} + \delta_{b})$.
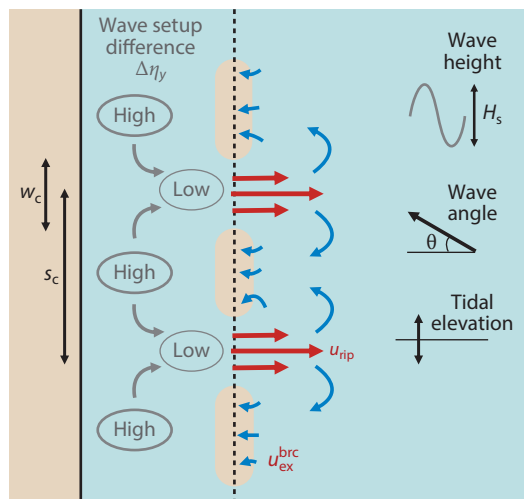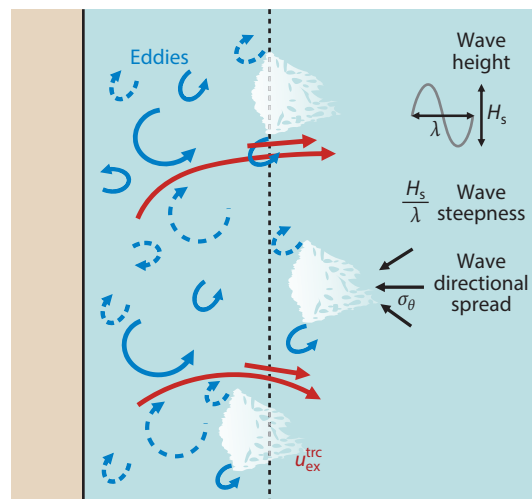
4.2. Bathymetric Rip Currents

The term rip currents describes several distinct phenomena resulting from wave breaking, including bathymetric rip currents that form in channels and transient (or flash) rip currents that result from multidirectional wavefields (Dalrymple et al. 2011, Castelle et al. 2016). What these features have in common is a narrow seaward jet with speeds up to several meters per second bounded laterally by slower, broader onshore return currents, leading to exchange of several centimeters per second up to a few surf-zone widths from shore. Rip currents thus efficiently connect the surf zone and the shelf with surf-zone flushing timescales of approximately tens of minutes to several hours.

Bathymetric rip currents form when waves break on sandbars that are cusped or channeled. For a sandbar that runs parallel to the shoreline and is interrupted by shore-perpendicular channels (alongshore spacing s_{c}, width w_{c}, and difference in depth on the bar and in the channel $\Delta h = h_{\text{chan}} - h_{\text{bar}}$), waves tend to break on the shallow shoals and not in the deeper channels (**Figure 7a**). This leads to elevated water-level setup onshore of the breaking regions, driving alongshore flows toward lower water levels in the channel and feeding an offshore-flowing rip current with speed u_{rip}.

Using Equation 6, bathymetric-rip-current-driven exchange is related to rip-current speed as $u_{\text{ex}}^{\text{brc}} \approx D_{r} u_{\text{rip}}$, where D_{r} is a rip-current density, the fraction of along-coast length occupied by rip-current jets. A reasonable upper bound on the density, assuming the jet width is smaller than or equal to the channel width, is the ratio of channel width and spacing, $D_{r} < w_{c}/s_{c}$, which can be estimated at a point in time or as a climatological average using bathymetric surveys or remote sensing (Holman & Haller 2013).

The speeds of bathymetric rip currents have been studied extensively in field, laboratory, numerical, and theoretical work and are typically larger for larger wave heights, lower tidal elevations, more shore-normal waves, and bathymetry that is more variable alongshore (Dalrymple et al. 2011, Castelle et al. 2016). The rip-current speed parameterization of Moulton et al. (2017) considers a pressure-head-driven flow, with $u_{\text{rip}} \approx F_{v}\sqrt{2g\Delta\eta_{y}}$, where the sea-level difference $\Delta\eta_{y}$ is governed by the pattern and strength of wave breaking (equation 4 in Moulton et al. 2017). The factor F_{v} (equation 6 in Moulton et al. 2017) is 1 when there is no alongshore current and as low as $\sim$0.5 for strong surf-zone alongshore currents, which can be driven by breaking waves approaching the beach at an angle, alongshore pressure gradients, or wind and are thought to suppress rip

a Bathymetric rip currents

b Transient rip currents

Figure 7

Top views of (*a*) bathymetric and (*b*) transient rip currents. Dashed lines mark the outer edge of the surf zone (*beach at left*). In panel *a*, wave breaking on shoals (*brown ellipses*) results in a higher mean water level onshore of the shoals ("high") than onshore of the deeper rip channels ("low"), where waves are not breaking, driving converging flows onshore of the channels (*gray arrows*), a seaward rip-current jet extending past the surf zone (*red arrows*), and onshore return currents (*blue arrows*). In panel *b*, breaking wave crests (*white*) inject counterclockwise and clockwise eddy circulation (*solid* and *dashed arrows*, respectively). Eddy interactions cause transient rip currents (*red arrows*).

currents. This effect is not well understood and may vary depending on the size of the bathymetry variations (Wilson et al. 2013).

The bathymetric rip-current exchange velocity is then

$$u_{\text{ex}}^{\text{brc}} \approx \begin{cases} 0, & \text{if } H_{\text{s,br}} < \gamma b_{\text{bar}} & \text{(shore break), 12a.} \\ D_{\text{r}} F_{\text{v}} \sqrt{2g\left[\frac{1}{16}\gamma^2\left(\cos^2\theta_{\text{br}} + \frac{1}{2}\right)(b_{\text{sz}} - b_{\text{bar}})\right]}, & \text{if } \gamma b_{\text{bar}} < H_{\text{s,br}} < \gamma b_{\text{chan}} \text{ (bar break),} & \text{12b.} \\ D_{\text{r}} F_{\text{v}} \sqrt{2g\left[\frac{1}{16}\gamma^2\left(\cos^2\theta_{\text{br}} + \frac{1}{2}\right)(b_{\text{chan}} - b_{\text{bar}})\right]}, & \text{if } H_{\text{s,br}} > \gamma b_{\text{chan}} & \text{(saturated),} & \text{12c.} \end{cases}$$

where the form depends on the pattern of wave breaking. There are no rip currents when smaller waves or higher tide lead to breaking only along the shoreline (shore break), while exchange increases with larger wave heights or lower tide when there is breaking on the bar (bar break). Note that $b_{\text{sz}} = H_{\text{s,br}}/\gamma$ is larger for larger offshore wave heights, and thus for bar-break conditions, $u_{\text{ex}}^{\text{brc}}$ increases with H_{s}. An upper bound on exchange is reached if breaking occurs even in the deeper channel (saturated surf-zone conditions).

In energetic conditions where wave breaking occurs on a variable bar, $H_{\text{s,br}} > \gamma b_{\text{bar}}$, a reasonable estimate of the maximum potential importance of bathymetric rip currents results from a simplification of the saturated case, assuming nearly shore-normal waves:

$$u_{\text{ex}}^{\text{brc,max}} \approx D_{\text{r}} \sqrt{2g\left(\frac{3}{32}\gamma^2\Delta b\right)} \quad \text{(maximum magnitude),} \qquad 13.$$

where typically $D_{\text{r}} \approx 0.01$–$0.1$ and $\Delta b \approx 0.2$–1.5 m, depending on the local bathymetry.

This estimate of bathymetric rip-current exchange is relevant at the outer edge of the surf zone. The cross-shore structure of bathymetric rip-current exchange has not been studied but likely decays offshore over several surf-zone widths, similar to transient rip currents (Section 4.3).

Velocity-based exchange (Equation 6) is straightforward to estimate from observed, modeled, or parameterized velocities and is a useful starting point for rip-current-driven offshore and onshore material transport. However, velocity-based exchange may overestimate the net exchange of surf-zone-originating particles to the shelf, in contrast to other metrics of exchange that consider particle trajectories, such as drifter exits and dye tracer balances that account for recirculation of ejected material back into the surf zone (MacMahan et al. 2010, Brown et al. 2015, Grimes et al. 2020).

4.3. Transient Rip Currents and Surf-Zone Eddies

Transient rip currents and surf-zone eddies form when alongshore wave-breaking gradients are caused by the wave field. This occurs in multidirectional wave conditions (Peregrine 1998) or when wave groups refract on bathymetric variability offshore of the surf zone (Long & Özkan-Haller 2009). Unlike the bathymetric rip-current case, where sandbar channels provide a persistent alongshore gradient (**Figure 7a**), in this case wave breaking is intermittent over the timescale of an individual wave (seconds) to that of a wave group (minutes) (**Figure 7b**).

Breaking wave crests that are finite in length (short-crested breaking; white in **Figure 7b**) are associated with a breaking force that varies alongshore, with strong forcing where the crest is breaking and no forcing in the adjacent region where there is no breaking. These intermittent gradients in wave breaking generate clockwise- and counterclockwise-rotating surf-zone eddies (Peregrine 1998, Bühler & Jacobson 2001). These eddies interact with each other, the varying bathymetry, and other currents, leading to a complex field of eddies with predominantly depth-uniform horizontal flow and horizontal sizes from meters to the width of the surf zone (hundreds of meters) (Spydell et al. 2009, Clark et al. 2010). The offshore flow associated with a pair of adjacent, counterrotating surf-zone-exiting eddies is described as a transient rip current (Johnson & Pattiaratchi 2004, Suanda & Feddersen 2015, Morgan et al. 2018b).

Within the surf zone, breaking waves and surf-zone eddies result in lateral mixing across the surf zone with an equivalent horizontal diffusivity similar to K_{ex} in Section 2.4. This surf-zone diffusivity is estimated through field studies with dye and drifter tracking (Spydell et al. 2007, Clark et al. 2010, Hally-Rosendahl et al. 2014) and numerical experiments (Spydell & Feddersen 2009, Spydell et al. 2019). The K_{ex} has a cross-shore profile that peaks around 1 m^2 s^{-1} in the middle of the surf zone and decays offshore. Thus, the rate of horizontal mixing is more rapid close to the shoreline relative to the outer surf zone (Spydell et al. 2019). Compared with other processes discussed in this review, horizontal mixing within the surf zone occurs rapidly (tens of minutes), due to the strength of breaking-wave-driven processes and because the surf zone is relatively narrow compared with the inner shelf.

In the transition region from the surf zone to the inner shelf, the eddy ejections known as transient rip currents drive exchange that can be related to bulk properties of the incident wave field. Kennedy (2005) predicted surf-zone eddy velocity on alongshore uniform coastlines to be most substantial for large and high-frequency waves with normally incident mean direction and large deep-water directional spread. Drifter and fixed-current-meter surf-zone observations suggest that the eddy field is affected by incoming significant wave height (Spydell et al. 2007) and mean wave incidence angle (Spydell et al. 2009). An increase in surf-zone eddy circulation associated with short-crested wave breaking has also been observed (Clark et al. 2012). Depth-averaged numerical model experiments across a wide range of beach slope and incident wave conditions (Suanda & Feddersen 2015) showed that the offshore rip-current exchange velocity (Equation 6) could be parameterized as

$$u_{ex}^{trc} = 0.03\sigma_{\theta,br}\sqrt{gb_{sz}}\,(1 + 70S_{br}), \qquad 14.$$

where S_{br} is the wave steepness at the break point, that is, the ratio between the offshore significant wave height and the wavelength at breaking, which is typically ~0.02 for small-to-moderate waves. In Equation 14, the exchange velocity in the middle of the surf zone (i.e., half the surf-zone width from the shoreline) is a function of the wave height via $h_{sz} = H_{s,br}/\gamma$, similar to the dependence for bathymetric rip currents. Unlike bathymetric rip currents, transient rip-current exchange also is a function of the wave directional spread at the offshore edge of the surf zone ($\sigma_{\theta,br}$ in radians in Equation 14), which is typically $10° < \sigma_{\theta,br} < 30°$ in the sea-swell frequency band (Herbers et al. 1999, O'Dea et al. 2021). The dependence of transient rip-current-driven exchange on mean wave angle has not been studied. The cross-shore profile of transient rip-current exchange is Gaussian and decays offshore from u_{ex}^{trc} (Equation 14) with a length scale associated with the beach slope and wave parameters at breaking. The value of u_{ex}^{trc} at the surf-zone edge, which may be most representative of exchange by transient rip-current ejections from the surf zone, is thus somewhat smaller than that given by Equation 14.

The u_{ex} scalings proposed above for rip currents assume approximately depth-uniform flows (Equations 6, 12, and 14), which is reasonable in the surf zone. Laboratory and field measurements, however, show that rip currents vary vertically farther offshore (Haas & Svendsen 2002, Hally-Rosendahl et al. 2014). Idealized numerical modeling shows that including vertical structure (Kumar & Feddersen 2016) and strong stratification (Kumar & Feddersen 2017a, Moulton et al. 2021) enhances rip-current exchange (Grimes & Feddersen 2021), indicating that future studies should work to incorporate these effects into u_{ex}.

4.4. Bottom Streaming

As surface waves propagate into shallow waters and interact with the seafloor, the phases of the horizontal and vertical components of the near-bottom wave orbital velocities shift such that they are no longer completely out of phase. This shift leads to a net flow in the wave bottom boundary layer known as bottom streaming (Longuet-Higgins 1953, Uchiyama et al. 2010, Trowbridge & Lentz 2018), usually toward shore, in the direction of wave propagation, which could return competent larvae to shore (Shanks 1995, Morgan et al. 2018a). The effects of bottom streaming are confined to the typically thin (millimeters to centimeters) wave bottom boundary layer and are sensitive to wave shape and other factors. For example, in the surf zone, where waves are asymmetric, bottom streaming can be directed offshore (Trowbridge & Madsen 1984). To be transported by bottom streaming, organisms and particles need strong downward velocities, or the ability to cling to the seabed, stay in the wave bottom boundary layer, and not be moved upward by turbulence. Even under small-to-moderate-wave conditions, a relatively large w_s is needed to compete with u^* in the bottom boundary layer. Simulating the impacts of bottom streaming is difficult, in part because including bottom streaming in a model that does not resolve the centimeters-thick wave bottom boundary layer can greatly overestimate its effects. An exchange velocity due to bottom streaming is not provided here, as new highly resolved measurements and modeling are needed to better understand the importance of this process.

5. INTERNAL WAVES AND TIDES

Coastal internal waves are generated predominantly offshore through interactions of the surface tide with bathymetric features such as the continental slope and shelf break (Baines 1982, Huthnance 1995). At offshore generation sites, tidally driven internal waves are typically linear (Section 5.1) and in phase with their tidal forcing (Kelly & Nash 2010). As internal waves propagate to shallower nearshore waters, the waves steepen and increase in amplitude, becoming increasingly nonlinear (**Figure 8**). These nonlinear internal waves can break into high-frequency
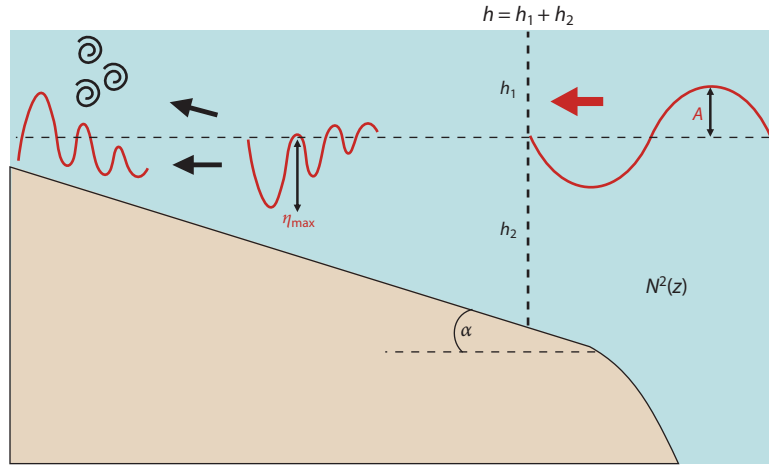
Figure 8

Internal waves evolving across the continental shelf. The dotted horizontal line indicates the unperturbed pycnocline. Linear internal waves [typical wavelength $\lambda \, \mathcal{O}(100 \text{ km})$ and period $\mathcal{O}(12.42 \text{ h})$] propagate toward the coast from offshore and evolve into a nonlinear internal wave train [$\lambda \, \mathcal{O}(100 \text{ m})$ and period $\mathcal{O}(10 \text{ min})$] and turbulence in the nearshore.

internal waves (solitary or in trains), tidal bores, or solibores—an intermediate between solitary waves and bores (sensu Lamb 2014). Nearshore internal wave arrivals are rarely in phase with the local surface tide (Nash et al. 2012).

A characteristic of internal waves is that the direction of horizontal velocities reverses with depth. The number of reversals corresponds to the vertical mode. Lower-mode internal waves propagate faster and farther from the generation site; they are therefore more commonly observed in the nearshore (Pringle & Brink 1999). Our review focuses on internal waves with a single current reversal (mode-1 waves): Their surface and bottom horizontal velocities are in opposition. In linear waves, horizontal velocities oscillate symmetrically over a wave period, resulting in a zero time-mean—or Eulerian-mean—flow at every depth. Nonlinear internal waves induce a nonzero Eulerian-mean flow: Waves of depression (isopycnals displaced downward) move surface waters onshore (Pineda 1999, Gough et al. 2020), while waves of elevation (isopycnals displaced upward) move bottom waters onshore (Bourgault et al. 2007).

In this section, exchange in linear, weakly nonlinear, and highly nonlinear internal waves is expressed as a particle transport distance per wave instead of an average velocity. This is because internal waves are intermittent and the time each particle spends in any given wave is not known a priori. To obtain an exchange velocity, the total onshore particle transport induced by many internal waves can be divided by the time over which these waves are observed. The development of parameterizations for the exchange associated with the nonlinear internal waves readily observed in the coastal ocean remains an active area of research, and at present exchange must be estimated numerically. Though we therefore cannot provide an explicit equation for u_{ex}, we have made code available online to estimate it in linear and weakly nonlinear waves (Garwood 2022, Moulton et al. 2022).

5.1. Internal Wave Parameters

To sample internal waves, a closely spaced vertical array of density measurements is most useful. Density time series can be used to estimate stratification, wave amplitude A (here defined as half

the wave height for both linear and nonlinear waves), and wave frequency ω. Stratification and water depth h can then be used to approximate the internal wave propagation speed c, from which wavelength λ or wavenumber k is calculated. Velocity measurements provide information on both wave-induced velocities u_w and background velocities. Internal waves can have frequencies as high as N (periods of approximately tens of minutes), and thus the sampling period should be <1 min. The internal wave vertical structure $\phi(z)$ can be estimated numerically from the observed background currents and stratification (Lian et al. 2020, 2022, which include code available online) or through empirical orthogonal function analysis of vertically and temporally resolved density observations (Inall et al. 2001, Garwood et al. 2021). In mode-1 internal waves, $\phi = 1$ at the location of horizontal current reversal, typically at the pycnocline. For constant N and no background currents, $\phi(z)$ is equal to $-\sin(\pi z/h)$.

The Froude number Fr characterizes both the extent of wave nonlinearity and the importance of wave-induced particle transport (Shanks 1995, Lamb 1997, Pineda 1999). When Fr is small ($Fr \ll 1$), internal waves are linear and particles are quickly left behind by a passing wave, thus experiencing limited wave-induced transport. When Fr is large, waves are nonlinear and particles can experience greater cross-shelf transport. Wave nonlinearity can also be estimated from the ratio of wave amplitude to water depth A/h, which is small for linear waves. The internal Iribarren number Ir can be an indicator of wave-breaking kinematics and transport over a sloping bottom (Boegman et al. 2005, Walter et al. 2012, Masunaga et al. 2017).

5.2. Material Transport by Internal Waves

In this section (and in many references therein), background currents are assumed to be negligible. However, depth-varying background currents—including any return flow associated with internal waves—can substantially modify the transport of plankton, especially those with depth-keeping behavior (Henderson 2016, Garwood et al. 2020a).

5.2.1. Linear waves. Linear internal waves induce horizontal transport of material through Stokes drift (Thorpe 1968, Spingys et al. 2020). As in surface waves (Section 4.1), drifting organisms moving with internal wave velocities experience a net displacement called Stokes drift (Garwood et al. 2020b) (**Figure 9a,b**). Previous authors have separated the contributions to Stokes drift due to particle horizontal and vertical motions (Henderson 2016, Franks et al. 2020). For a mode-1 internal wave in uniform stratification, the Stokes drift velocity is

$$u_{\text{Stokes,IW}}(z) = \frac{A^2 \pi^2 \omega}{2kh^2} \cos \frac{2\pi z}{h}. \qquad 15.$$

5.2.2. Weakly nonlinear waves. Whereas material transport in linear waves is due only to Stokes drift, transport in nonlinear waves is caused by both the nonzero mean (wave-averaged) flow and Stokes drift. There is no clear cutoff regarding what Fr values separate linear and nonlinear internal waves, but weakly nonlinear theory describes waves with $A/h \sim 0.1$–0.3 well (Shroyer et al. 2010, Zhang et al. 2015, Garwood et al. 2020a).

Transport of surface-trapped particles in solitary waves can be estimated from theory, but transport distance estimates for particles throughout the water column require numerical modeling (Lamb 1997). Ideally, dynamical internal wave models should be used (Lamb 2002, Scotti et al. 2008), but first-order estimates can be obtained by advecting particles in observed wave velocities or in velocities derived from a prescribed wave shape that resembles observations (e.g., cosine, cosine squared, or hyperbolic secant) and using an estimated wave propagation speed (Garwood et al. 2020b). When assuming a wave shape is not practical, measurements of the time-varying,

c: internal wave speed; for a constant N, $c = Nh/\pi$, and for a two-layer fluid, $c = \left(\frac{g'h_1 h_2}{h_1 + h_2}\right)^{1/2}$, where $g' = g\frac{\rho_2 - \rho_1}{\rho_2}$, ρ_1 and ρ_2 are the upper- and lower-layer water density, respectively, and h_1 and h_2 are the upper- and lower-layer thickness, respectively

Froude number (Fr): ratio of wave-induced horizontal velocities to wave propagation speed; $Fr = u_w/c$

Internal Iribarren number (Ir): ratio of the bathymetric slope (α) to the square root of the internal wave steepness (internal wave amplitude A divided by wavelength λ); $Ir = \alpha/\sqrt{A/\lambda}$
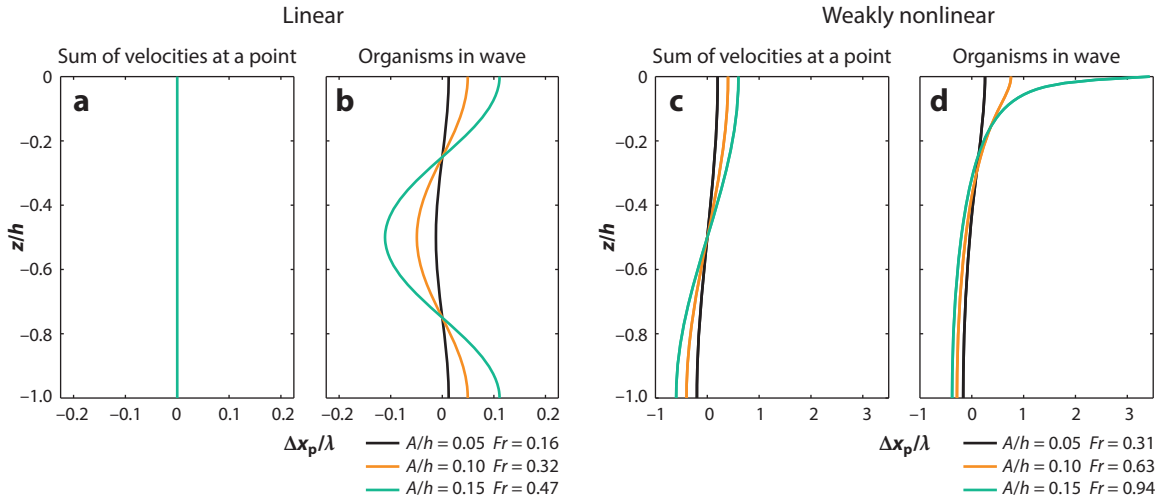
Figure 9

Particle transport distances in (*a,b*) linear or (*c,d*) weakly nonlinear (solitary) internal waves, calculated from (*a,c*) time integration of modeled velocity at a fixed depth, (*b*) using Equation 15, and (*d*) advecting Lagrangian particles. Note that equal *A/h* values yield distinct *Fr* (calculated at the surface) in linear versus weakly nonlinear waves. The horizontal axis scale is 10 times smaller for linear waves. Code to reproduce or modify this figure and the underlying analysis is available at **https://doi.org/10.5281/zenodo.6784256** (Garwood 2022).

vertical isopycnal displacement can be used to estimate exchange (Inall et al. 2001). However, this approach does not advect particles and therefore neglects Stokes drift.

Figure 9 provides estimates of cross-shore particle transport distances associated with linear and weakly nonlinear internal waves that propagate in uniform stratification, following Garwood et al. (2020b). Time-integrating velocities at a given depth neglects Stokes drift and vertical particle motions, thus underestimating particle transport (compare **Figure 9*a,b*** or **Figure 9*c,d***). At low $Fr \leq 0.3$, the transport distances estimated from such integration (black line in **Figure 9*c***) are similar to the transport distances estimated by advecting particles (black line in **Figure 9*d***). However, as *Fr* increases, integrating velocities at a fixed depth grossly underestimates transport distances, particularly near the surface (Zhang et al. 2015) (teal lines in **Figure 9*c,d***).

5.2.3. Highly nonlinear internal waves and bores. Linear and weakly nonlinear theories provide first-order estimates of cross-shelf particle exchange, but coastal internal waves are often highly nonlinear and include particle trapping and wave-breaking dynamics (Lamb 2014, Woodson 2018, Davis et al. 2020). Highly nonlinear internal waves, such as internal bores, are asymmetric and steep and can have poorly defined wavelengths or amplitudes. In these waves, wave-induced velocities approach the wave propagation speed ($Fr \rightarrow 1$), so fluid (and any particles within it) is trapped and travels with the wave. Trapping conditions, however, can be difficult to predict (Lamb 2003). Furthermore, breaking internal waves both generate and advect turbulence (Moum et al. 2007, Richards et al. 2013, Becherer et al. 2020), influencing stratification through mixing. Separating wave influences and background conditions is particularly challenging (Winters et al. 1995; McSweeney et al. 2020, 2021).

Due to the complexity of real-world ocean conditions, much of the research on material transport in bores comes from idealized laboratory (Boegman & Stastna 2019) and numerical experiments. A numerical study by Arthur & Fringer (2016) considered a single solitary internal wave

propagating in a two-layer fluid over a uniformly sloping beach with no alongshore variations. In their simulations, shoreward particle transport occurs within an upslope surge of dense bottom fluid after wave breaking, while offshore transport occurs within an intermediate layer in the middle of the water column, where bottom fluid has mixed with less dense surface water. These dynamics could sustain intermediate nepheloid (sediment-laden) layers (McPhee-Shaw 2006, Masunaga et al. 2017). Both onshore and offshore particle transport distances Δx_p scale inversely with Ir (Arthur & Fringer 2016). Breaking waves on a moderate slope ($Ir < 1$) displace near-bed particles approximately one wavelength toward the shore (approximately hundreds of meters, or $\Delta x_p/\lambda = 1$ in **Figure 9**) and displace middepth particles a similar distance in the offshore direction. Steeper bathymetric slopes or less steep waves ($Ir > 1$) result in particle transport distances of less than one wavelength.

5.2.4. Impact of behavior.

Both horizontal and vertical swimming can influence how organisms interact with wave velocities and have implications for particle cross-shore transport. Horizontal swimming modifies a larva's realized Fr, with swimming in the direction of wave propagation increasing the time larvae stay with the wave, resulting in greater transport distances (Shanks 1995, Lamb 1997, Pineda 1999, Helfrich & Pineda 2003).

In this review, the ability of larvae to maintain depth was often assessed by comparing swimming and turbulent vertical velocities because other vertical fluid velocities were small. The vertical velocities caused by internal waves, however, can be $\mathcal{O}(1\text{--}10 \text{ cm s}^{-1})$, comparable to or larger than larval swimming speeds. Therefore, the ability of a larva to maintain depth is set by its swimming speed relative to the wave vertical velocities and any turbulence (see Section 2.3): $w_s/(w_w + u^*_{\text{total}})$. Steeper and more turbulent internal waves are a more challenging environment for depth-keeping plankton. While maintaining depth or swimming vertically, larvae cross isopycnals as internal waves heave isopycnals past the larvae. Thus, larvae sample the shear associated with waves (and displaced background velocities) differently than passive organisms, resulting in cross-shore displacements that vary with swimming ability (Franks et al. 2020; Garwood et al. 2020a, 2021). The transport of plankton with perfect depth-keeping ability in linear internal waves, for instance, can be estimated from a modification of Equation 15 by setting the contribution to Stokes drift of vertical motions to zero (Franks et al. 2020):

$$u_{\text{Stokes,IW}}(z) = \frac{A^2 \pi^2 \omega}{2kh^2} \cos^2 \left(\frac{\pi z}{h} \right). \qquad 16.$$

Larvae with instantaneous responses and speeds that exceed wave vertical velocities can maintain depth and experience maximum onshore displacements. However, because the vertical velocities encountered by larvae moving with the wave are different from those measured at a mooring, and because vertical velocities fluctuate over a wave period, larvae with much weaker swimming speeds than the maximum Eulerian wave vertical velocity can also experience maximum displacements (Franks et al. 2020, Garwood et al. 2021).

6. DIURNAL HEATING AND COOLING

In most coastal oceans, the solar day/night cycle drives diurnal ocean heating and cooling (e.g., Austin 1999). Heating makes the water less dense, and cooling makes it more dense. If turbulent mixing does not reach the bottom, then the heating and cooling affect only surface waters, do not create horizontal density gradients in the surface mixed layer, and thus do not drive horizontal motions (Mahadevan et al. 2010). In the nearshore, if mixing extends to the bottom during warming and cooling, or if solar radiative heating extends to the bottom, the daily cycle of heating and

cooling can set up cross-shelf density gradients that drive cross-shelf flows. When the surface heat flux warms the ocean, the shallower part of the nearshore heats up faster, setting up a gradient in temperature (warmer toward the coast) and density (denser farther offshore). When there is surface cooling, the opposite occurs. Alternating periods of heating and cooling set up alternating on- and offshore density gradients, which drive alternate periods of downwelling and upwelling overturning flows (Monismith et al. 2006, Molina et al. 2014, Safaie et al. 2022).

Exchange due to diurnal heating and cooling is present when there is a strong, fluctuating surface heat flux and sufficiently strong mixing from winds or alongshore currents. Mixing is strong enough to overcome the stratifying effects of heating when the u^* associated with surface or bottom stresses is larger than the w^* associated with the maximum heat flux (Stull 1988) (see the sidebar titled Sources of Turbulence in the Nearshore). When vertical mixing is strong, the cross-shelf transport of heat is relatively weak (Monismith et al. 2006), as there is little temperature difference between the surface and bottom (Ulloa et al. 2018). The heat balance is approximately one-dimensional (vertical), and the change in temperature relative to an initial state is determined by the time integral of the local heat flux distributed over the water depth: $T = \frac{1}{h c_p \rho_0} \int Q \, dt$. The resulting cross-shelf temperature gradient is proportional to the gradient in water depth: $\frac{\partial T}{\partial x} = -\frac{1}{h^2 c_p \rho_0} \frac{\partial h}{\partial x} \int Q \, dt$. In the absence of salinity variations, the cross-shelf density gradient is $\frac{\partial \rho}{\partial x} = -\alpha_T \rho_0 \frac{\partial T}{\partial x}$. This density gradient sets up a baroclinic pressure gradient force that is balanced primarily by turbulent mixing of momentum through the water column (Ulloa et al. 2018); the associated vertical eddy viscosity is approximately $A_v = \frac{1}{4} \kappa u^*_{total} h$ (Lentz 1995). This leads to an exchange flow with a magnitude $u_{ex}^{diurnal} \approx \frac{g}{6 A_v \rho_0} h^3 \frac{\partial \rho}{\partial x}$. The near-surface flow is toward the denser water, and the near-bottom flow is in the opposite direction (**Figure 10**). The shallow region closest to the coast is most dense following the period of maximum cooling and least dense following the period of maximum heating, and thus the surface flows are most strongly offshore at the end of the day and most strongly onshore at the end of the night.

Given a scale for the surface heat flux Q_{mag} of half the difference between the maximum and minimum heat flux, the magnitude of the time-integrated heat flux is approximately $Q_{mag} T_{day}/\pi$
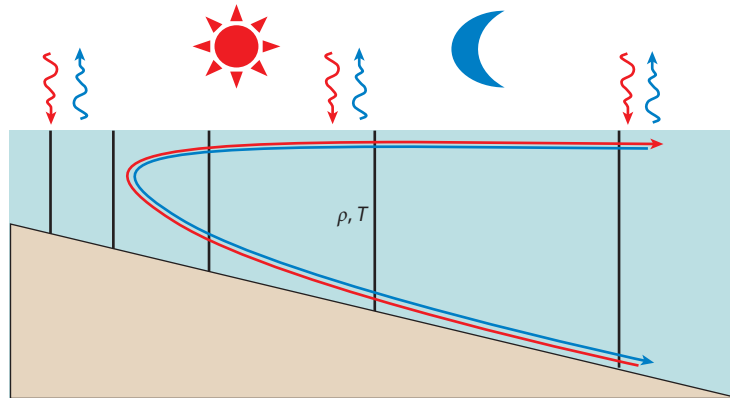

Figure 10

Horizontal gradients in density and resulting exchange flow associated with diurnal heating and cooling. Temperature (*black isotherms*) is vertically uniform and varies horizontally, with greater gradients (*smaller spacing between isotherms*) in shallower water. After daytime heating (*red*), warmer (less dense) water is found in shallower water, driving offshore flow near the surface and onshore flow at depth. After nighttime cooling (*blue*), cooler (denser) water is found in shallower water, driving onshore flow near the surface and offshore flow at depth.

(the integral of a sinusoidal heat flux over half a day; T_{day} is a day), and the cross-shelf density gradient magnitude is $\left|\frac{\partial \rho}{\partial x}\right| \approx \frac{\alpha_T}{\pi h^2 c_p} \frac{\partial h}{\partial x} Q_{mag} T_{day}$. The magnitude of the exchange velocity is then

$$u_{ex}^{diurnal} = \frac{2}{3} \frac{g \alpha_T T_{day}}{\rho_0 \pi c_p \kappa u_{total}^*} \frac{\partial h}{\partial x} Q_{mag}. \qquad 17.$$

Because the density gradient scales as h^{-2}, u scales as h^3, and the mixing scales as h, the exchange velocity does not vary with increasing water depth until the water becomes deep enough that the surface heat flux is not mixed to the bottom and this mechanism becomes unimportant.

7. APPLICATION TO CENTRAL CALIFORNIA

Here, the cross-shore exchange framework is applied to quantify the relative importance of nearshore exchange processes off central California north of Point Conception, a region of the California Current upwelling system with a rich history of oceanic observations (e.g., Melton et al. 2009, Washburn et al. 2011, Fewings et al. 2015, Aristizábal et al. 2016, Kumar et al. 2021, and references below). Two cases typical of fall conditions are considered: one with a strongly stratified shelf, light winds, and small surface waves (case 1), and another with an unstratified or weakly stratified water column, high winds, and waves large enough to be unsafe for small-boat sampling (case 2). As outlined in Section 2, for each case, the strength of stratification and boundary-layer thicknesses are assessed to determine candidate exchange processes. For this example, a buoyant particle or near-surface depth-keeping organism with strong swimming relative to turbulent velocity fluctuations $w_s > 0.25 u_{total}^*$ is considered, such that the exchange velocity u_{ex} (Equations 5 and 6) is a good metric for how fast particles move in one direction across the shelf (Section 2.3). For particles that are mixed through the water column, a similar approach could be applied to estimate horizontal exchange diffusivities K_{ex} (Equation 4).

In the fall on the central California coast, wind events are typically moderate (4–10 m s^{-1}) and upwelling-favorable and last 2–5 days, followed by wind relaxations (e.g., Dorman & Winant 2000). Surface waves propagate dominantly from the northwest, with $T_p = 8$–10 s, $H_s = 1$–3 m, and $\sigma_\theta = 25°$ on the 20-m isobath (O'Dea et al. 2021). Although shelf stratification is weak compared with that of the neighboring Santa Barbara Channel (Aristizábal et al. 2017), vertical temperature gradients are on average 0.02–0.1°C m^{-1} at the 10–15-m isobath (Suanda et al. 2017, Feddersen et al. 2020), with the potential to support internal waves and suppress turbulence (Cudaback & McPhee-Shaw 2009, Colosi et al. 2018, McSweeney et al. 2020). Internal tides are the dominant source of observed semidiurnal internal variability at this location (Aristizábal et al. 2017, Colosi et al. 2018, Kumar et al. 2019), and average internal wave amplitudes are 10–15% of the water column depth (Colosi et al. 2018, McSweeney et al. 2020). The typical peak daytime surface heat flux is ~600–800 W m^{-2}, and the nearshore bathymetry on sandy parts of the coastline is characterized by an approximately 1-m-high bar with channels spaced every 100–500 m (O'Dea et al. 2021).

7.1. Strongly Stratified with a Light Breeze and a Small Swell (Case 1)

Following the flowchart in **Figure 2**, case 1 considers a strongly stratified shelf ($dT/dz = 0.3°C$ m^{-1}) with $Ri_{bulk} > 0.65$, leading to box i in **Figure 2b** (**Figure 11a**). During times with relatively weak winds ($|\tau_s| = 0.03$ N m^{-2}, from the northwest), the surface and bottom boundary layers on the shelf are relatively thin ($\delta_s \approx 9$ m). The cross-shore and alongshore winds are important drivers of exchange velocity over much of the nearshore; the wind speeds are low, but stratification and small wind stress confine the transport to a thin surface boundary layer, leading to a larger
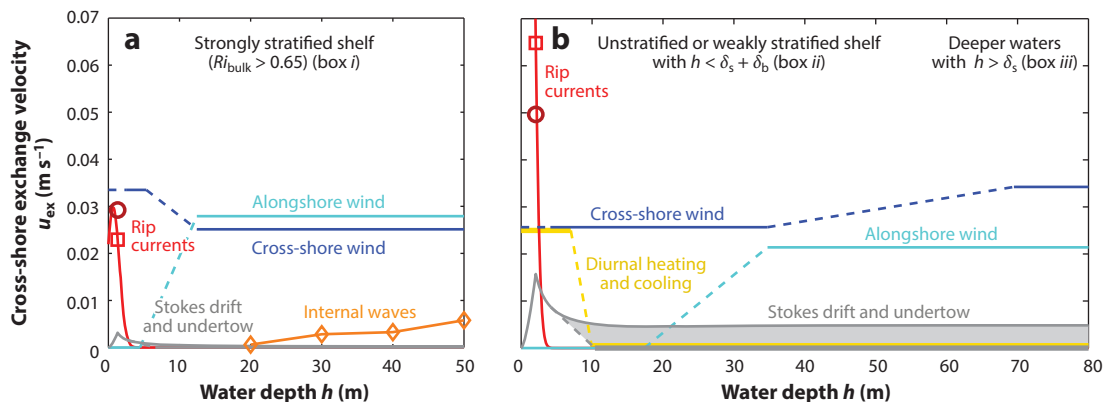
Figure 11

The relative importance of cross-shore exchange processes as a function of water depth or cross-shore position (Kumar diagrams). Two forcing scenarios on the central California coast in fall are considered: (*a*) a strongly stratified shelf with weak wind and waves (case 1; Section 7.1) and (*b*) an unstratified or weakly stratified shelf during a relatively strong wind and wave event (case 2; Section 7.2). Boxes *i*, *ii*, and *iii* refer to the flowchart boxes in **Figure 2b**. Exchange velocities u_{ex} (the unsigned magnitude of cross-shore exchange) are compared for rip currents (transient, *red curve and square* at the edge of the surf zone; bathymetric, *dark red circle*), Stokes drift and undertow (with *gray shading* indicating a possible range), cross-shore (*blue*) and alongshore (*cyan*) wind, internal waves (*orange*), and diurnal heating and cooling (*yellow*). Dashed curves indicate transitions between regions. The relative magnitudes shown here are an example for a particular set of environmental conditions and thus cannot be directly applied to other study regions or seasons. Code to reproduce or modify this figure and the underlying analysis is available at **https://doi.org/10.5281/zenodo.6816225** (Moulton et al. 2022).

exchange velocity for these strongly swimming or buoyant organisms. To estimate $u_{ex}^{wind,cross-shelf}$ for these strongly stratified conditions ($N^2 = 10^{-4}$ s^{-2}), we use $B = 0.9$ in Equation 9a (Tilburg 2003, Lentz & Fewings 2012). Alongshore winds do not contribute appreciably to cross-shore exchange where $h < \delta_s$. Note that for near-surface particles in the thin surface Ekman layer, obtaining the wind-driven u_{ex} by averaging above the first zero crossing is reasonable, but a depth-keeping particle in the middle of the water column may actually experience weak or zero cross-shore displacement due to winds in this case.

Even during these smaller-swell conditions ($H_{br} = 0.95$ m, $T_p = 11$ s, $\sigma_{\theta,br} = 8°$), surface wave–driven exchange can still be comparable to other processes. For weak vertical mixing on the shelf ($h > \sim 4$ m, more than a few widths of the surf zone from shore), the onshore Stokes drift is balanced by the offshore-directed undertow at all vertical levels and results in no net exchange. However, even under stratified shelf conditions, the surf-zone region ($h < 1.3$ m) is well mixed, and thus Stokes drift and undertow contribute a net exchange, with magnitude controlled by the decreasing height of the breaking waves. Near the edge of the surf zone, bathymetric rip currents are expected to contribute substantially to exchange, even for these relatively small wave heights. A low-tide case is considered here, but at the highest tides, these small waves may not break on the bar, resulting in a bathymetric rip-current exchange equal to zero. Exchange driven by transient rip currents is smaller due to the small directional spread, and it decays offshore within two surf-zone widths, where density gradients may begin to affect exchange.

Shoreward-propagating internal waves are supported by the stratification and may be a significant exchange process in this case, based on the average wave properties and number of waves per day reported by Colosi et al. (2018). For these conditions, internal waves contribute significantly to exchange in water depths of 30–50 m, whereas few waves make it into shallower water depths, and their contribution to exchange is smaller than that of winds and rip currents. No

diurnally reversing exchange flow driven by heating and cooling occurs for this case, at least outside of the surf zone, as stratification prevents diurnal mixed layers caused by nighttime cooling from reaching the bottom.

7.2. Unstratified, Windy, and Wavy Enough for a Small-Craft Warning (Case 2)

Again following the flowchart in **Figure 2b**, case 2 considers an unstratified or weakly stratified shelf during a relatively strong wind event, leading to boxes *ii* and *iii* (**Figure 11b**). Under these conditions ($|\tau_s| = 0.15$ N m^{-2}, from the northwest), the wind-driven exchange is similar in pattern but smaller than the stratified case, despite stronger wind stress, due to the larger boundary-layer thickness ($\delta_s \approx 58$ m). Note that cross-shore wind-driven exchange velocities for these near-surface depth-keeping particles are larger than those for alongshore winds everywhere. By contrast, when considering total surface-layer volume transport rather than an exchange velocity, alongshore winds have greater importance in deeper water (Lentz & Fewings 2012).

Despite relatively strong mixing, observational and theoretical evidence points to Stokes drift and undertow approximately balancing at all vertical levels over most of the shelf (**Figure 11b**, gray curve at 0 m s^{-1} in >10-m depth), except very near the surf zone (Section 4.1). However, there is some debate about whether Stokes drift and undertow may have a net exchange very near the surface (**Figure 11b**, gray curve at 0.005 m s^{-1}). This gray area in the literature is represented with the shaded gray area in **Figure 11b**. Where u_{ex}^{Stokes} is nonzero, its magnitude is larger than in case 1, due to more energetic and steeper waves ($H_{br} = 1.5$ m, $T_p = 7$ s). The exchange velocity due to Stokes drift and undertow peaks at the edge of the surf zone ($h \approx 2$ m). The exchange associated with transient rip currents is stronger in case 2 than in case 1, in part due to larger wave directional spread ($\sigma_{\theta,br} = 20°$). Exchange from bathymetric rip currents is also larger than in case 1, but the scale of bathymetric variability limits the maximum exchange. Both cases assume the beach is channeled ($\Delta h = 1$ m) and that wave directions are shore-normal ($\theta = 0°$); cases with more uniform sandbars or strong longshore currents would have weaker rip currents. Internal waves are not supported in case 2 due to the unstratified or weakly stratified environment. Finally, diurnal heating and cooling can become important near the coast. Assuming a peak heating of 650 W m^{-2}, w^* is less than u^* in depths less than 7 m, where wind-driven turbulence can prevent even daytime heating from stratifying the water column, thus allowing diurnal heating and cooling to drive cross-shelf exchange. Assuming the difference between daytime warming and nighttime cooling is $\sim$850 W m^{-2}, $u_{ex}^{diurnal}$ is approximately 2.5 cm s^{-1}, comparable to the values for other exchange processes.

7.3. Ecological Implications

The emphasis of this review has been to identify which processes may be important to moving particles across the nearshore at a given location and time, whether that exchange is likely to be rapid or slow, and whether expected particle motion is best described by movement in one direction or spreading both onshore and offshore. For a more detailed assessment of implications for the cross-shore distribution of particles, initial distributions of plankton, pollutants, or particles could be advected in a high-resolution numerical model that includes all relevant processes (Section 8.2). Alternatively, a qualitative estimate of the cross-shore distribution of particles or plankton could be obtained by considering a signed sum of exchange velocities. For example, if for case 1 the winds were offshore and upwelling-favorable, then because offshore wind-driven exchanges outweigh all other exchange mechanisms, a patch of surface-keeping larvae initially at some offshore location would likely not reach the beach and instead would move farther offshore. However, if instead particle swimming was weak and turbulence mixed the particles throughout

the water column, the initial patch of particles would spread in the cross-shore direction both offshore and onshore. Some particles could therefore reach the edge of the surf zone, where they would spread rapidly due to the strong action of rip currents and surf-zone processes, and some particles could reach the beach. If winds shifted to onshore and downwelling, the entire patch could be delivered to the edge of the surf zone, allowing a larger number of the particles to reach the shore. These dynamics and interactions emphasize the importance of particle behavior and other factors in determining ecological outcomes, such as the timing of spawning events relative to changes in local wind and wave forcing (Section 8.3).

8. FUTURE DIRECTIONS

8.1. Building on the Exchange Velocity and Diffusivity Framework

In our example application of the exchange velocity framework (Section 7), we focused on how the relative importance of different processes varies with cross-shore position and time. However, the exchange velocity framework could also reasonably be used to assess how process importance varies along a coast. For example, for wind and waves coming from the northwest, a more northward-facing stretch of coastline may have stronger rip currents and cross-shore-wind-driven exchange than a more southward-facing beach a few tens of kilometers away. Because our framework generally assumes alongshore uniformity, applying it to assess alongshore changes in cross-shore exchange is sensible only for mechanisms that are relatively local, which may be reasonable for rip currents and cross-shore winds but less so for alongshore winds (Brink et al. 1987, Pringle 2002). More work is needed to understand when exchange processes are affected by alongshore variability (e.g., Largier 2020).

In addition, several processes, including those controlled by alongshore variability in the bathymetry and coastline, were not included in this review, in part because they lack a well-defined exchange velocity formulation. Headlands impinging on alongshore flows, such as flows driven by tides or winds, can cause the flow to separate from the coast and create transient or persistent fronts and eddies that contribute strongly to localized cross-shore transport and retention of particles (Morgan et al. 2009, Woodson et al. 2012, Romero et al. 2013, Kovatch et al. 2021). Both headland eddies and coastal fronts are associated with submesoscale instabilities and filaments that can drive cross-shore exchange and mixing (Dauhajre et al. 2017, Wang et al. 2021, Wu et al. 2021). Future work is needed to parameterize the contributions of these processes to exchange. More work is also needed to understand potential barriers to nearshore exchange, which could result from simultaneous opposing processes, surface convergences associated with single or multiple processes, or other effects (Ohlmann et al. 2012, Restrepo et al. 2014, McWilliams 2018). Finally, the interactions among processes affect exchange and should be investigated further. For example, the strength and structure of rip-current-driven exchange may be modulated by the interaction with stratification (Kumar & Feddersen 2017b), internal waves, or freshwater sources.

8.2. Inclusion of Underresolved Processes in Numerical Models

Regional numerical models, which typically have horizontal resolutions of $\mathcal{O}(1\ \text{km})$ or larger, often do not resolve the nearshore processes discussed here within the grid cells adjacent to land. As such, particles that reach these final grid cells are commonly assumed to have a fixed probability of reaching land (beaching) or settling in a nearshore water depth (e.g., Drake et al. 2011, Delandmeter & van Sebille 2019, Pawlowicz 2020), neglecting important variability. Parameterizing exchange processes in the coastal grid cells based on nearshore dynamics, rather than a fixed probability, may be a useful improvement. Such a parameterization could be forced by the modeled stratification and vertical turbulence profiles from the coastal grid cells, surface

and internal wave fluxes from offshore, and wind stress. This approach could provide an analytical estimate of the cross-shelf exchange, or probability of exchange, of particles across the unresolved nearshore region as a function of resolved ocean conditions and assigned particle behavior.

8.3. Organisms That React to the Environment

Our framework focused on passive or depth-keeping particles but ignored ontogenetic changes in behavior or responses to ocean conditions. This view is simplified, for many larvae react to fluctuating environmental stimuli, and these responses could have evolved to increase cross-shore transport toward suitable adult habitats (e.g., Fuchs et al. 2018). The inclusion of these refined interactions in estimates of transport across the nearshore is limited by our understanding of both what plankton can sense and their responses. In the future, the framework introduced here could be used to inform how a larva's sensing ability can be coupled with changes in vertical swimming to modulate cross-shelf transport (Garwood et al. 2022).

SUMMARY POINTS

1. An exchange velocity u_{ex} is used to estimate the strength of material exchange across the nearshore region due to winds, Stokes drift and undertow, bathymetric and transient rip currents, internal waves, and diurnal heating and cooling.

2. The ratio of particle and turbulent vertical velocity magnitudes is used to assess the effect of behavior on exchange. If $w_s/u^*_{total} > 0.25$, net particle transport scales with u_{ex}. Otherwise, particles are mixed vertically and spread both onshore and offshore at a slower rate characterized by a horizontal diffusivity K_{ex}, which is a function of u_{ex} and the vertical turbulent mixing.

3. Future work could extend this framework to other processes and alongshore-varying coasts, develop exchange parameterizations at the coastal boundary of numerical models, and include impacts of organisms adjusting their swimming behavior in response to turbulence and other ocean conditions.

DISCLOSURE STATEMENT

The authors are not aware of any affiliations, memberships, funding, or financial holdings that might be perceived as affecting the objectivity of this review.

ACKNOWLEDGMENTS

Section 7 were gathered as part of the ONR Inner-Shelf Dynamics Experiment (**https://doi.org/10.6075/J0WD3Z3Q**).

We are thankful for the many hours spent talking about science (and everything else) with wonderful colleagues, including Nirnimesh Kumar (1984–2020), who continues to inspire us: *Like as the waves make towards the pebbl'd shore / . . . / And yet to times in hope [our] verse shall stand* (Shakespeare, sonnet 60, lines 1 and 13). We thank one anonymous reviewer and early readers Robert Arthur (Lawrence Livermore National Laboratory), Jennifer L. Fisher (NOAA Northwest Fisheries Science Center, Newport, Oregon), Peter Franks (Scripps Institution of Oceanography), Derek Grimes (University of North Carolina Wilmington), Steven Lentz (Woods Hole Oceanographic Institution), and Parker MacCready (University of Washington) for helpful feedback.

LITERATURE CITED

Aristizábal MF, Fewings MR, Washburn L. 2016. Contrasting spatial patterns in the diurnal and semidiurnal temperature variability in the Santa Barbara Channel, California. *J. Geophys. Res. Oceans* 121:427–40

Aristizábal MF, Fewings MR, Washburn L. 2017. Effects of the relaxation of upwelling-favorable winds on the diurnal and semidiurnal water temperature fluctuations in the Santa Barbara Channel, California. *J. Geophys. Res. Oceans* 122:7958–77

Arthur RS, Fringer OB. 2016. Transport by breaking internal gravity waves on slopes. *J. Fluid Mech.* 789:93–126

Austin JA. 1999. The role of the alongshore wind in the heat balance of the North Carolina inner shelf. *J. Geophys. Res. Oceans* 104:39888–902

Austin JA, Lentz SJ. 2002. The inner shelf response to wind-driven upwelling and downwelling. *J. Phys. Oceanogr.* 32:2171–93

Baines PG. 1982. On internal tide generation models. *Deep-Sea Res. A* 29:307–38

Battjes JA, Janssen JPFM. 1978. Energy loss and set-up due to breaking of random waves. In *Proceedings of the 16th Conference on Coastal Engineering*, pp. 569–87. Reston, VA: Am. Soc. Civil Eng.

Becherer J, Moum JN, Colosi JA, Lerczak JA, McSweeney JM. 2020. Turbulence asymmetries in bottom boundary layer velocity pulses associated with onshore-propagating nonlinear internal waves. *J. Phys. Oceanogr.* 50:2373–91

Boegman L, Ivey GN, Imberger J. 2005. The degeneration of internal waves in lakes with sloping topography. *Limnol. Oceanogr.* 50:1620–37

Boegman L, Stastna M. 2019. Sediment resuspension and transport by internal solitary waves. *Annu. Rev. Fluid Mech.* 51:129–54

Boehm AB, Ismail NS, Sassoubre LM, Andruszkiewicz EA. 2017. Oceans in peril: grand challenges in applied water quality research for the 21st century. *Environ. Eng. Sci.* 34:3–15

Bourgault D, Blokhina MD, Mirshak R, Kelley DE. 2007. Evolution of a shoaling internal solitary wavetrain. *Geophys. Res. Lett.* 34:L03601

Bowden KF. 1965. Horizontal mixing in the sea due to a shearing current. *J. Fluid Mech.* 21:83–95

Brasseale E, MacCready P. 2021. The shelf sources of estuarine inflow. *J. Phys. Oceanogr.* 51:2407–21

Brink KH. 2016. Cross-shelf exchange. *Annu. Rev. Mar. Sci.* 8:59–78

Brink KH, Chapman DC, Halliwell GR Jr. 1987. A stochastic model for wind-driven currents over the continental shelf. *J. Geophys. Res. Oceans* 92:1783–97

Brink KH, Lentz SJ. 2009. Buoyancy arrest and bottom Ekman transport. Part I: steady flow. *J. Phys. Oceanogr.* 40:621–35

Brown JA, MacMahan JH, Reniers AJ, Thornton ED. 2015. Field observations of surf zone-inner shelf exchange on a rip-channeled beach. *J. Phys. Oceanogr.* 45:2339–55

Bühler O, Jacobson TE. 2001. Wave-driven currents and vortex dynamics on barred beaches. *J. Fluid Mech.* 449:313–39

Castelle B, Scott T, Brander R, McCarroll R. 2016. Rip current types, circulation and hazard. *Earth-Sci. Rev.* 163:1–21

CIESIN (Cent. Int. Earth Sci. Inf. Netw.). 2012. *National aggregates of geospatial data collection: population, landscape, and climate estimates, version 3 (PLACE III)*. Data Set, NASA Socioecon. Data Appl. Cent., Palisades, NY. **https://doi.org/10.7927/H4F769GP**

Clark DB, Elgar S, Raubenheimer B. 2012. Vorticity generation by short-crested wave breaking. *Geophys. Res. Lett.* 39:L24604

Clark DB, Feddersen F, Guza RT. 2010. Cross-shore surfzone tracer dispersion in an alongshore current. *J. Geophys. Res. Oceans* 115:C10035

Clarke AJ, Van Gorder S. 2018. The relationship of near-surface flow, Stokes drift and the wind stress. *J. Geophys. Res. Oceans* 123:4680–92

Colford JM Jr., Schiff KC, Griffith JF, Yau V, Arnold BF, et al. 2012. Using rapid indicators for *Enterococcus* to assess the risk of illness after exposure to urban runoff contaminated marine water. *Water Res.* 46:2176–86

Colosi JA, Kumar N, Suanda SH, Freismuth TM, MacMahan JH. 2018. Statistics of internal tide bores and internal solitary waves observed on the inner continental shelf off Point Sal, California. *J. Phys. Oceanogr.* 48:123–43

Cowen RK, Sponaugle S. 2009. Larval dispersal and marine population connectivity. *Annu. Rev. Mar. Sci.* 1:443–66

Cudaback CN, McPhee-Shaw E. 2009. Diurnal-period internal waves near Point Conception, California. *Estuar. Coast. Shelf Sci.* 83:349–59

Dalrymple RA, MacMahan JH, Reniers AJ, Nelko V. 2011. Rip currents. *Annu. Rev. Fluid Mech.* 43:551–81

Dauhajre DP, McWilliams JC, Uchiyama Y. 2017. Submesoscale coherent structures on the continental shelf. *J. Phys. Oceanogr.* 47:2949–76

Davis KA, Arthur RS, Reid EC, Rogers JS, Fringer OB, et al. 2020. Fate of internal waves on a shallow shelf. *J. Geophys. Res. Oceans* 125:e2019JC015377

Delandmeter P, van Sebille E. 2019. The Parcels v2.0 Lagrangian framework: new field interpolation schemes. *Geosci. Model Dev.* 12:3571–84

Dorman CE, Winant CD. 2000. The structure and variability of the marine atmosphere around the Santa Barbara Channel. *Mon. Weather Rev.* 128:261–82

Drake PT, Edwards CA, Barth JA. 2011. Dispersion and connectivity estimates along the US west coast from a realistic numerical model. *J. Mar. Res.* 69:1–37

Edson JB, Jampana V, Weller RA, Bigorre SP, Plueddemann AJ, et al. 2013. On the exchange of momentum over the open ocean. *J. Phys. Oceanogr.* 43:1589–610

Elko N, Feddersen F, Foster D, Hapke CJ, McNinch JE, et al. 2015. The future of nearshore processes research. *Shore Beach* 83(1):13–38

Estrade P, Marchesiello P, De Verdière AC, Roy C. 2008. Cross-shelf structure of coastal upwelling: a two-dimensional extension of Ekman's theory and a mechanism for inner shelf upwelling shut down. *J. Mar. Res.* 66:589–616

Feddersen F, MacMahan JH, Freismuth TM, Gough MK, Kovatch M. 2020. Inner-shelf vertical and alongshore temperature variability in the subtidal, diurnal, and semidiurnal bands along the central California coastline with headlands. *J. Geophys. Res. Oceans* 125:e2019JC015347

Feddersen F, Trowbridge JH, Williams AJ. 2007. Vertical structure of dissipation in the nearshore. *J. Phys. Oceanogr.* 37:1764–77

Fewings MR, Lentz SJ, Fredericks J. 2008. Observations of cross-shelf flow driven by cross-shelf winds over the inner continental shelf. *J. Phys. Oceanogr.* 38:2358–78

Fewings MR, Washburn L, Ohlmann JC. 2015. Coastal water circulation patterns around the Northern Channel Islands and Point Conception, California. *Prog. Oceanogr.* 138:283–304

Franks PJS, Garwood JC, Ouimet M, Cortes J, Musgrave RC, Lucas AJ. 2020. Stokes drift of plankton in linear internal waves: cross-shore transport of neutrally buoyant and depth-keeping organisms. *Limnol. Oceanogr.* 65:1286–96

Fredsoe J, Deigaard R. 1992. *Mechanics of Coastal Sediment Transport*. Singapore: World Sci.

Fuchs HL, Gerbi GP, Hunter EJ, Christman AJ. 2018. Waves cue distinct behaviors and differentiate transport of congeneric snail larvae from sheltered versus wavy habitats. *PNAS* 115:E7532–40

Garcez Faria AF, Thornton EB, Lippmann TC, Stanton TP. 2000. Undertow over a barred beach. *J. Geophys. Res. Oceans* 105:16999

Garwood JC. 2022. Tools to generate particle tracks in linear and weakly nonlinear internal waves. *Zenodo*. **https://doi.org/10.5281/zenodo.6784256**

Garwood JC, Fuchs HL, Gerbi GP, Hunter EJ, Chant RJ, Wilkin JL. 2022. Estuarine retention of larvae: contrasting effects of behavioral responses to turbulence and waves. *Limnol. Oceanogr.* 67:992–1005

Garwood JC, Lucas AJ, Naughton P, Alford MH, Roberts PLD, et al. 2020a. A novel cross-shore transport mechanism revealed by subsurface, robotic larval mimics: internal wave deformation of the background velocity field. *Limnol. Oceanogr.* 65:1456–70

Garwood JC, Lucas AJ, Naughton P, Roberts PLD, Jaffe JS, et al. 2021. Larval cross-shore transport estimated from internal waves with a background flow: the effects of larval vertical position and depth regulation. *Limnol. Oceanogr.* 66:678–93

Garwood JC, Musgrave R, Lucas A. 2020b. Life in internal waves. *Oceanography* 33(3):38–49

Geyer WR, MacCready P. 2014. The estuarine circulation. *Annu. Rev. Fluid Mech.* 46:175–97

Gough MK, Freismuth TM, MacMahan JH, Colosi JA, Suanda SH, Kumar N. 2020. Heating of the midshelf and inner shelf by warm internal tidal bores. *J. Phys. Oceanogr.* 50:2609–20

Grantham BA, Chan F, Nielsen KJ, Fox DS, Barth JA, et al. 2004. Upwelling-driven nearshore hypoxia signals ecosystem and oceanographic changes in the northeast Pacific. *Nature* 429:749–54

Grimes DJ, Feddersen F. 2021. The self-similar stratified inner-shelf response to transient rip-current-induced mixing. *J. Fluid Mech.* 915:A82

Grimes DJ, Feddersen F, Kumar N. 2020. Tracer exchange across the stratified inner-shelf driven by transient rip-currents and diurnal surface heat fluxes. *Geophys. Res. Lett.* 47:e2019GL086501

Haas KA, Svendsen IA. 2002. Laboratory measurements of the vertical structure of rip currents. *J. Geophys. Res. Oceans* 107:15-1–19

Hally-Rosendahl K, Feddersen F, Guza RT. 2014. Cross-shore tracer exchange between the surfzone and inner-shelf. *J. Geophys. Res. Oceans* 119:4367–88

Hasselmann K, Barnett TP, Bouws E, Carlson H, Cartwright DE, et al. 1973. *Measurements of Wind-Wave Growth and Swell Decay During the Joint North Sea Wave Project (JONSWAP)*. Hamburg, Ger.: Dtsch. Hydrogr. Inst.

Helfrich K, Pineda J. 2003. Accumulation of particles in propagating fronts. *Limnol. Oceanogr.* 48:1509–20

Henderson SM. 2016. Upslope internal-wave Stokes drift, and compensating downslope Eulerian mean currents, observed above a lakebed. *J. Phys. Oceanogr.* 46:1947–61

Herbers THC, Elgar S, Guza RT. 1999. Directional spreading of waves in the nearshore. *J. Geophys. Res. Oceans* 104:7683–93

Holman RA, Haller MC. 2013. Remote sensing of the nearshore. *Annu. Rev. Mar. Sci.* 5:95–113

Horner-Devine AR, Hetland RD, MacDonald DG. 2015. Mixing and transport in coastal river plumes. *Annu. Rev. Fluid Mech.* 47:569–94

Horwitz R, Lentz SJ. 2014. Inner-shelf response to cross-shelf wind stress: the importance of the cross-shelf density gradient in an idealized numerical model and field observations. *J. Phys. Oceanogr.* 44:86–103

Horwitz RM, Lentz SJ. 2016. The effect of wind direction on cross-shelf transport on an initially stratified inner shelf. *J. Mar. Res.* 74:201–27

Huthnance JM. 1995. Circulation, exchange and water masses at the ocean margin: the role of physical processes at the shelf edge. *Prog. Oceanogr.* 35:353–431

Inall ME, Shapiro GI, Sherwin TJ. 2001. Mass transport by non-linear internal waves on the Malin Shelf. *Cont. Shelf Res.* 21:1449–72

Johnson D, Pattiaratchi C. 2004. Transient rip currents and nearshore circulation on a swell-dominated beach. *J. Geophys. Res. Oceans* 109:C02026

Kelly SM, Nash JD. 2010. Internal-tide generation and destruction by shoaling internal tides. *Geophys. Res. Lett.* 37:L23611

Kennedy AB. 2005. Fluctuating circulation forced by unsteady multidirectional breaking waves. *J. Fluid Mech.* 538:189–98

Kirincich A, Lentz S, Barth J. 2009. Wave-driven inner-shelf motions on the Oregon coast. *J. Phys. Oceanogr.* 39:2942–56

Kovatch M, Feddersen F, Grimes DJ, MacMahan JH. 2021. Vorticity recirculation and asymmetric generation at a small headland with broadband currents. *J. Geophys. Res. Oceans* 126:e2020JC016639

Kumar N, Cahl DL, Crosby SC, Voulgaris G. 2017. Bulk versus spectral wave parameters: implications on Stokes drift estimates, regional wave modeling, and HF radars applications. *J. Phys. Oceanogr.* 47:1413–31

Kumar N, Feddersen F. 2016. The effect of Stokes drift and transient rip currents on the inner shelf. Part II: with stratification. *J. Phys. Oceanogr.* 47:243–60

Kumar N, Feddersen F. 2017a. The effect of Stokes drift and transient rip currents on the inner shelf. Part I: no stratification. *J. Phys. Oceanogr.* 47:227–41

Kumar N, Feddersen F. 2017b. A new offshore transport mechanism for shoreline-released tracer induced by transient rip currents and stratification. *Geophys. Res. Lett.* 44:2843–51

Kumar N, Lerczak JA, Xu T, Waterhouse AF, Thomson J, et al. 2021. The Inner-Shelf Dynamics Experiment. *Bull. Am. Meteorol. Soc.* 102:E1033–63

Kumar N, Suanda SH, Colosi JA, Haas K, Di Lorenzo E, et al. 2019. Coastal semidiurnal internal tidal incoherence in the Santa Maria Basin, California: observations and model simulations. *J. Geophys. Res. Oceans* 124:5158–79

Lamb KG. 1997. Particle transport by nonbreaking, solitary internal waves. *J. Geophys. Res.* 102:18641

Lamb KG. 2002. A numerical investigation of solitary internal waves with trapped cores formed via shoaling. *J. Fluid Mech.* 451:109–44

Lamb KG. 2003. Shoaling solitary internal waves: on a criterion for the formation of waves with trapped cores. *J. Fluid Mech.* 478:81–100

Lamb KG. 2014. Internal wave breaking and dissipation mechanisms on the continental slope/shelf. *Annu. Rev. Fluid Mech.* 46:231–54

Largier JL. 2020. Upwelling bays: how coastal upwelling controls circulation, habitat, and productivity in bays. *Annu. Rev. Mar. Sci.* 12:415–47

Lentz SJ. 1995. Sensitivity of the inner-shelf circulation to the form of the eddy viscosity profile. *J. Phys. Oceanogr.* 25:19–28

Lentz SJ, Chapman DC. 2004. The importance of nonlinear cross-shelf momentum flux during wind-driven coastal upwelling. *J. Phys. Oceanogr.* 34:2444–57

Lentz SJ, Fewings MR. 2012. The wind- and wave-driven inner-shelf circulation. *Annu. Rev. Mar. Sci.* 4:317–43

Lentz SJ, Fewings MR, Howd P, Fredericks J, Hathaway K. 2008. Observations and a model of undertow over the inner continental shelf. *J. Phys. Oceanogr.* 38:2341–57

Lentz SJ, Raubenheimer B. 1999. Field observations of wave setup. *J. Geophys. Res. Oceans* 104:25867–75

Li Q, Fox-Kemper B. 2017. Assessing the effects of Langmuir turbulence on the entrainment buoyancy flux in the ocean surface boundary layer. *J. Phys. Oceanogr.* 47:2863–86

Lian Q, Smyth WD, Liu Z. 2020. Numerical computation of instabilities and internal waves from in situ measurements via the viscous Taylor-Goldstein problem. *J. Atmos. Ocean. Technol.* 37:759–76

Lian Q, Smyth WD, Liu Z. 2022. Matlab tools to solve the viscous Taylor Goldstein equation for both instabilities and waves. *Zenodo*. **https://doi.org/10.5281/zenodo.6516994**

Long JW, Özkan-Haller HT. 2009. Low-frequency characteristics of wave group–forced vortices. *J. Geophys. Res. Oceans* 114:C08004

Longuet-Higgins MS. 1953. Mass transport in water waves. *Philos. Trans. R. Soc. A* 245:535–81

Longuet-Higgins MS, Stewart RW. 1964. Radiation stresses in water waves; a physical discussion, with applications. *Deep-Sea Res. Oceanogr. Abstr.* 11:529–62

MacKinnon JA, Gregg MC. 2005. Spring mixing: turbulence and internal waves during restratification on the New England shelf. *J. Phys. Oceanogr.* 35:2425–43

MacMahan JH, Brown JW, Brown JA, Thornton EB, Reniers AJHM, et al. 2010. Mean Lagrangian flow behavior on an open coast rip-channeled beach: a new perspective. *Mar. Geol.* 268:1–15

Madsen O. 1977. A realistic model of the wind-induced Ekman boundary layer. *J. Phys. Oceanogr.* 7:248–55

Mahadevan A, Tandon A, Ferrari R. 2010. Rapid changes in mixed layer stratification driven by submesoscale instabilities and winds. *J. Geophys. Res. Oceans* 115:C03017

Masunaga E, Arthur RS, Fringer OB, Yamazaki H. 2017. Sediment resuspension and the generation of intermediate nepheloid layers by shoaling internal bores. *J. Mar. Syst.* 170:31–41

McCabe RM, Hickey BM, Dever EP, MacCready P. 2015. Seasonal cross-shelf flow structure, upwelling relaxation, and the alongshelf pressure gradient in the Northern California Current System. *J. Phys. Oceanogr.* 45:209–27

McPhee-Shaw E. 2006. Boundary–interior exchange: reviewing the idea that internal-wave mixing enhances lateral dispersal near continental margins. *Deep-Sea Res. II* 53:42–59

McSweeney JM, Fewings MR, Lerczak JA, Barth JA. 2021. The evolution of a northward-propagating buoyant coastal plume after a wind relaxation event. *J. Geophys. Res. Oceans* 126:e2021JC017720

McSweeney JM, Lerczak JA, Barth JA, Becherer J, MacKinnon JA, et al. 2020. Alongshore variability of shoaling internal bores on the inner shelf. *J. Phys. Oceanogr.* 50:2965–81

McWilliams JC. 2018. Surface wave effects on submesoscale fronts and filaments. *J. Fluid Mech.* 843:479–517

Melton C, Washburn L, Gotschalk C. 2009. Wind relaxations and poleward flow events in a coastal upwelling system on the central California coast. *J. Geophys. Res. Oceans* 114:C11016

Molina L, Pawlak G, Wells JR, Monismith SG, Merrifield MA. 2014. Diurnal cross-shore thermal exchange on a tropical forereef. *J. Geophys. Res. Oceans* 119:6101–20

Monismith SG. 2019. Stokes drift: theory and experiments. *J. Fluid Mech.* 884:F1

Monismith SG, Genin A, Reidenbach MA, Yahel G, Koseff JR. 2006. Thermally driven exchanges between a coral reef and the adjoining ocean. *J. Phys. Oceanogr.* 36:1332–47

Morgan SG, Fisher JL, Miller SH, McAfee ST, Largier JL. 2009. Nearshore larval retention in a region of strong upwelling and recruitment limitation. *Ecology* 90:3489–502

Morgan SG, Miller SH, Robart MJ, Largier JL. 2018a. Nearshore larval retention and cross-shelf migration of benthic crustaceans at an upwelling center. *Front. Mar. Sci.* 5:161

Morgan SG, Shanks AL, MacMahan JH, Reniers AJ, Feddersen F. 2018b. Planktonic subsidies to surf-zone and intertidal communities. *Annu. Rev. Mar. Sci.* 10:345–69

Moulton M, Chickadel CC, Thomson J. 2021. Warm and cool nearshore plumes connecting the surf zone to the inner shelf. *Geophys. Res. Lett.* 48:e2020GL091675

Moulton M, Elgar S, Raubenheimer B, Warner JC, Kumar N. 2017. Rip currents and alongshore flows in single channels dredged in the surf zone. *J. Geophys. Res. Oceans* 122:3799–816

Moulton M, Suanda SH, Garwood JC, Kumar N, Fewings MR, Pringle JM. 2022. Nearshore-exchange toolbox. *Zenodo*. **https://doi.org/10.5281/zenodo.6816225**

Moum JN, Klymak JM, Nash JD, Perlin A, Smyth WD. 2007. Energy transport by nonlinear internal waves. *J. Phys. Oceanogr.* 37:1968–88

Nash JD, Kelly SM, Shroyer EL, Moum JN, Duda TF. 2012. The unpredictable nature of internal tides on continental shelves. *J. Phys. Oceanogr.* 42:1981–2000

O'Dea A, Kumar N, Haller MC. 2021. Simulations of the surf zone eddy field and cross-shore exchange on a nonidealized bathymetry. *J. Geophys. Res. Oceans* 126:e2020JC016619

Ohlmann JC, Fewings MR, Melton C. 2012. Lagrangian observations of inner-shelf motions in Southern California: Can surface waves decelerate shoreward-moving drifters just outside the surf zone? *J. Phys. Oceanogr.* 42:1313–26

Pawlowicz R. 2020. The grounding of floating objects in a marginal sea. *J. Phys. Oceanogr.* 51:537–51

Pearson B. 2018. Turbulence-induced anti-Stokes flow and the resulting limitations of large-eddy simulation. *J. Phys. Oceanogr.* 48:117–22

Peregrine DH. 1998. Surf zone currents. *Theor. Comput. Fluid Dyn.* 10:295–309

Pineda J. 1999. Circulation and larval distribution in internal tidal bore warm fronts. *Limnol. Oceanogr.* 44:1400–14

Pineda J, Reyns N. 2018. Larval transport in the coastal zone: biological and physical processes. In *Evolutionary Ecology of Marine Invertebrate Larvae*, ed. TJ Carrier, AM Reitzel, A Heyland, pp. 145–63. Oxford, UK: Oxford University Press

Pollard RT, Rhines PB, Thompson RORY. 1972. The deepening of the wind-mixed layer. *Geophys. Astrophys. Fluid Dyn.* 4:381–404

Price J, Weller R, Pinkel R. 1986. Diurnal cycling: observations and models of the upper ocean response to heating, cooling, and wind mixing. *J. Geophys. Res. Oceans* 91:8411–27

Pringle JM. 2002. Enhancement of wind-driven upwelling and downwelling by alongshore bathymetric variability. *J. Phys. Oceanogr.* 32:3101–12

Pringle JM. 2022. JamiePringle/NearshoreParticleTransport: release v1.0.0. *Zenodo*. **https://doi.org/10.5281/zenodo.6812919**

Pringle JM, Brink KH. 1999. High frequency internal waves on a sloping shelf. *J. Geophys. Res. Oceans* 104:5283–99

Pringle JM, Franks PJ. 2001. Asymmetric mixing transport: a horizontal transport mechanism for sinking plankton and sediment in tidal flows. *Limnol. Oceanogr.* 46:381–91

Prüss A. 1998. Review of epidemiological studies on health effects from exposure to recreational water. *Int. J. Epidemiol.* 27:1–9

Raubenheimer B, Guza RT, Elgar S. 2001. Field observations of wave-driven setdown and setup. *J. Geophys. Res. Oceans* 106:4629–38

Restrepo JM, Venkataramani SC, Dawson C. 2014. Nearshore sticky waters. *Ocean Model.* 80:49–58

Richards C, Bourgault D, Galbraith PS, Hay A, Kelley DE. 2013. Measurements of shoaling internal waves and turbulence in an estuary. *J. Geophys. Res. Oceans* 118:273–86

Rilov G, Dudas SE, Menge BA, Grantham BA, Lubchenco J, Schiel DR. 2008. The surf zone: a semi-permeable barrier to onshore recruitment of invertebrate larvae? *J. Exp. Mar. Biol. Ecol.* 361:59–74

Romero L, Uchiyama Y, Ohlmann JC, McWilliams JC, Siegel DA. 2013. Simulations of nearshore particle-pair dispersion in Southern California. *J. Phys. Oceanogr.* 43:1862–79

Safaie A, Pawlak G, Davis KA. 2022. Diurnal thermally driven cross-shore exchange in steady alongshore currents. *J. Geophys. Res. Oceans* 127:e2021JC017912

Savidge DK, Gargett AE. 2017. Langmuir supercells on the middle shelf of the South Atlantic Bight: 1. Cell structure. *J. Mar. Res.* 75:49–79

Scotti A, Beardsley RC, Butman B, Pineda J. 2008. Shoaling of nonlinear internal waves in Massachusetts Bay. *J. Geophys. Res. Oceans* 113:C08031

Shanks AL. 1995. Orientated swimming by megalopae of several eastern North Pacific crab species and its potential role in their onshore migration. *J. Exp. Mar. Biol. Ecol.* 186:1–16

Shroyer EL, Moum JN, Nash JD. 2010. Vertical heat flux and lateral mass transport in nonlinear internal waves. *Geophys. Res. Lett.* 37:L08601

Spingys CP, Williams RG, Hopkins JE, Hall RA, Green JAM, Sharples J. 2020. Internal tide-driven tracer transport across the continental slope. *J. Geophys. Res. Oceans* 125:e2019JC015530

Spydell MS, Feddersen F. 2009. Lagrangian drifter dispersion in the surf zone: directionally spread, normally incident waves. *J. Phys. Oceanogr.* 39:809–30

Spydell MS, Feddersen F, Guza RT. 2009. Observations of drifter dispersion in the surfzone: the effect of sheared alongshore currents. *J. Geophys. Res. Oceans* 114:C07028

Spydell MS, Feddersen F, Guza RT, Schmidt WE. 2007. Observing surf-zone dispersion with drifters. *J. Phys. Oceanogr.* 37:2920–39

Spydell MS, Feddersen F, Suanda SH. 2019. Inhomogeneous turbulent dispersion across the nearshore induced by surfzone eddies. *J. Phys. Oceanogr.* 49:1015–34

Stull RB. 1988. *An Introduction to Boundary Layer Meteorology.* Boston: Kluwer Acad.

Suanda SH, Feddersen F. 2015. A self-similar scaling for cross-shelf exchange driven by transient rip currents. *Geophys. Res. Lett.* 42:2015GL063944

Suanda SH, Feddersen F, Kumar N. 2017. The effect of barotropic and baroclinic tides on coastal stratification and mixing. *J. Geophys. Res. Oceans* 122:10156–73

Terray EA, Donelan MA, Agrawal YC, Drennan WM, Kahma KK, et al. 1996. Estimates of kinetic energy dissipation under breaking waves. *J. Phys. Oceanogr.* 26:792–807

Thorpe S. 1968. On the shape of progressive internal waves. *Philos. Trans. R. Soc. A* 263:563–614

Tilburg CE. 2003. Across-shelf transport on a continental shelf: Do across-shelf winds matter? *J. Phys. Oceanogr.* 33:2675–88

Trowbridge J, Madsen OS. 1984. Turbulent wave boundary layers: 2. Second-order theory and mass transport. *J. Geophys. Res. Oceans* 89:7999–8007

Trowbridge JH, Lentz SJ. 2018. The bottom boundary layer. *Annu. Rev. Mar. Sci.* 10:397–420

Uchiyama Y, McWilliams JC, Shchepetkin AF. 2010. Wave-current interaction in an oceanic circulation model with a vortex-force formalism: application to the surf zone. *Ocean Model.* 34:16–35

Ulloa HN, Davis KA, Monismith SG, Pawlak G. 2018. Temporal variability in thermally driven cross-shore exchange: the role of semidiurnal tides. *J. Phys. Oceanogr.* 48:1513–31

van den Bremer TS, Breivik Ø. 2017. Stokes drift. *Philos. Trans. R. Soc. A* 376:20170104

Walter RK, Squibb ME, Woodson CB, Koseff JR, Monismith SG. 2014. Stratified turbulence in the nearshore coastal ocean: dynamics and evolution in the presence of internal bores. *J. Geophys. Res. Oceans* 119:8709–30

Walter RK, Woodson CB, Arthur RS, Fringer OB, Monismith SG. 2012. Nearshore internal bores and turbulent mixing in southern Monterey Bay. *J. Geophys. Res. Oceans* 117:C07017

Wang P, McWilliams JC, Uchiyama Y. 2021. A nearshore oceanic front induced by wave streaming. *J. Phys. Oceanogr.* 51:1967–84

Washburn L, Fewings MR, Melton C, Gotschalk C. 2011. The propagating response of coastal circulation due to wind relaxations along the central California coast. *J. Geophys. Res. Oceans* 116:C12028

Weatherly GL, Martin PJ. 1978. On the structure and dynamics of the oceanic bottom boundary layer. *J. Phys. Oceanogr.* 8:557–70

Wilson GW, Özkan-Haller HT, Holman RA. 2013. Quantifying the length-scale dependence of surf zone advection. *J. Geophys. Res. Oceans* 118:2393–407

Winters KB, Lombard PN, Riley JJ, D'Asaro EA. 1995. Available potential energy and mixing in density-stratified fluids. *J. Fluid Mech.* 289:115–28

Woodson CB. 2018. The fate and impact of internal waves in nearshore ecosystems. *Annu. Rev. Mar. Sci.* 10:421–41

Woodson CB, McManus MA, Tyburczy JA, Barth JA, Washburn L, et al. 2012. Coastal fronts set recruitment and connectivity patterns across multiple taxa. *Limnol. Oceanogr.* 57:582–96

Wu X, Feddersen F, Giddings SN. 2021. Characteristics and dynamics of density fronts over the inner to midshelf under weak wind conditions. *J. Phys. Oceanogr.* 51:789–808

Zhang S, Alford MH, Mickett JB. 2015. Characteristics, generation, and mass transport of nonlinear internal waves on the Washington continental shelf. *J. Geophys. Res. Oceans* 120:741–58